DEM study on the dynamic responses of a ballasted track under moving loading

Jing Chen[a,b], Jayan S. Vinod[b,*], Buddhima Indraratna[c], Trung Ngo[c], Yangzepeng Liu[a]

[a]*School of Civil Engineering, Wuhan University, Wuhan 430072, China*

[b]*Faculty of Engineering and Information Sciences, University of Wollongong, Wollongong City, NSW 2522, Australia*

[c]*Transport Research Centre, Faculty of Engineering and Information Technology, University of Technology Sydney, Sydney, NSW 2007, Australia*

ABSTRACT: This paper presents the discrete element modeling of the dynamic response of a ballasted track under moving loads. The DEM model, consisting of sleepers, ballast, and sub-ballast, has been calibrated using field and laboratory data. This model was further used to examine the dynamic responses of the ballasted track subjected to a series of moving traffic loading representing various train axle loads and speeds. The results show that the permanent settlement of the sleeper, the breakage of ballast, and the dynamic stresses in the track substructure increase with an increase in train axle load and speed. As the train moves, the magnitudes of dynamic stresses and the orientations of principal stress axes in the track change continuously, and a more pronounced principal stress rotation is observed at sleeper edges than those underneath sleepers. The capping layer is found to play a critical role in reducing train-induced stress and further alleviating the disturbance from the trains to the subgrade. The interparticle contacts and the vibration of ballast during the movement of the train including the influences of train axle load and speed on the dynamic responses of ballasted railway tracks are captured and analyzed from a micromechanical perspective.

Keywords: Ballast breakage; Sleeper settlement; Moving loading; Discrete element method; Principal stress rotation

1. Introduction

The ballasted track is a traditional form of railway structure commonly used worldwide due to its low construction cost and high adaptability to the environment. As the main substructure components of the track, ballast and sub-ballast provide a stable platform for the superstructure (sleepers, fasteners,

*Corresponding author
Email address: vinod@uow.edu.au (Jayan S. Vinod)

and rails) and help distribute the induced high-level trainload to the underlying soil subgrade (Indraratna et al., 2011; Selig and Waters, 1994). With the increasing use of faster and heavier trains in recent decades, track-related problems such as differential settlements or ballast fouling have become increasingly prominent. Consequently, these issues not only increase high maintenance costs for ballasted railways but also pose significant threats to the stability and operation safety of railway tracks. Understanding the dynamic responses of ballasted tracks under actual train loading conditions is vital for securing the long-term viability of the tracks and ensuring the sustainability of the railway system.

There have been numerous laboratory studies to investigate the mechanical behavior of ballast using direct shear tests (Huang et al., 2009; Indraratna et al., 2014; Jing et al., 2020), cyclic triaxial tests (Bian et al., 2016; Qian et al., 2015), and cubical box tests (Indraratna et al., 2013; McDowell et al., 2005). Through these experimental approaches, the mechanical properties and responses of ballast aggregates (i.e., shear stress-strain behavior) under predetermined loading conditions can be fundamentally understood. However, most of the applied loads in laboratory tests were simplified to either monotonic loads or sinusoidal cyclic loads, which are somehow different from the actual moving loads encountered in the typical ballasted bed. Field studies (Zhang et al., 2017; Zhao et al., 2021) have indicated that the dynamic stress generated by one single bogie at the sleeper-ballast interface is usually in the complex 'M' shape, and this 'M' shaped stress pulse has been reported to significantly affect the responses of rail tracks. In addition, ballast aggregates in most of the existing studies were statically loaded, which runs counter to the successively moving traffic loads in actual railways. The moving load would continuously rotate the principal stress axes and change the stress states in track layers. It has been proven that the principal stress rotation (PSR) could significantly affect the responses of aggregates, such as their permanent deformation, shear stiffness, non-coaxiality (Cai et al., 2008a, 2008b; Gräbe and Clayton, 2009; Qian et al., 2019).

There have been various studies to investigate the detrimental effect of the moving load on the deformation of the ballasted track using full-scale railway model testing facilities (Aursudkij et al., 2009; Momoya et al., 2005). Numerical studies were also carried out using the traditional Finite Element Method (FEM) to investigate the impact of various influencing factors including the modulus and thicknesses of track substructure layers, the amplitude of train moving loads, and the train speed on the dynamic response of ballasted railway track-ground systems (Sayeed and Shahin, 2022). (Zhao et al., 2021) performed a series of FEM analyses and numerically explored the moving load effect on subgrade soil in railway tracks. (Malisetty et al., 2020; Punetha and Nimbalkar, 2022) have adopted mathematical approaches to study the effect of PSR on the track response. However, most of the existing laboratory testing and numerical analysis are restrained to the exploration of the macroscopic performance of subgrade soils, whereas the dynamic response of ballast aggregates under moving train loading needs to be investigated from the particulate scale.

Over the past decades, various analytical methods within the framework of non-continuum mechanics have been proposed and developed to examine the behavior of discontinuous ballast aggregates, among which the discrete element modeling (DEM) pioneered by (Cundall and Strack, 1979) has been widely adopted by railway researchers (Chen et al., 2022; Liu et al., 2019; McDowell and Li, 2016; Ngo and Indraratna, 2020). By using the DEM, (Bian et al., 2020) presented a ballasted track model to study the effect of principal stress rotation (PSR) on track settlement. (Feng et al., 2019) created a full-scale DEM model equipped with ballast aggregates and eight crossties, and investigated the transient particle moving tendencies in ballast layer during train moving. In conventional DEM applications, physical objects are normally simulated as rigid elements that cannot be able to produce any elastic deformation or degradation.

To overcome the abovementioned problems, some coupled numerical methods that combine the advantages of continuum-based methods such as the finite element method (FEM) with the DEM have been developed. (Munjiza, 2004) proposed the combined finite-discrete element method (FDEM), and it has been successfully applied to study the fracture and fragmentation of rockfill materials. However, owing to the large computational resources required for solving the global matrices and parallel computing, the FDEM is mostly used for the quasi-static analysis of individual particles or assemblies containing a limited number of grains. (Sakaguchi, 2004) developed the quadruple discrete element method (QDEM) as an alternative approach to the FDEM with its superiority in high-efficient parallelization to capture the long-term analysis of multi-body structures. (Nishiura et al., 2017, 2018) investigated the characteristics of frequency vibration for ballasted tracks under cyclic loading using QDEM. Although these FEM-based analytical methods can be used to evaluate the dynamic phenomena for elastic/viscoelastic geomaterials, such as elastic deformation, natural vibration, and wave propagation, their application in the long-term dynamic response analysis of ballasted track is still limited due to the high requirements in parallel computing. Hence, there still exist some insufficiencies in studies on the related topics. First and foremost, the degradation (breakage) of ballast aggregate and its influence on the settlement of superstructures (sleepers) are not investigated. Besides, the degradation and deformation of the ballast layer under moving loading conditions (varied train speeds and axle loads) are not explored. Moreover, the fundamental mechanism of dynamic aggregate-superstructure interaction for railway infrastructure remains unknown and requires to be understood from a microscopic perspective.

Considering the abovementioned inadequacies in these approaches, a series of numerical simulations are carried out using the DEM to examine the dynamic responses of ballasted tracks under moving traffic loading. The sleeper settlement, the ballast degradation, and the dynamic stress distribution of ballast beds subjected to various traffic loading with different axle loads and speeds are captured and analyzed. In-depth microscopic analysis is also provided from a particulate scale in terms of interparticle contact and ballast vibration velocity of ballasted tracks during train passage.

2. Discrete Element Modeling of Ballast Track

2.1 Modeling of ballasted track beds

A traditional ballasted track system typically consists of the following components: (a) steel rail and fastening system, (b) sleepers or ties, (c) ballast aggregates, (d) capping layer (sub-ballast), and (e) subgrade, as shown in Fig. 1(a) and Fig. 1(b).

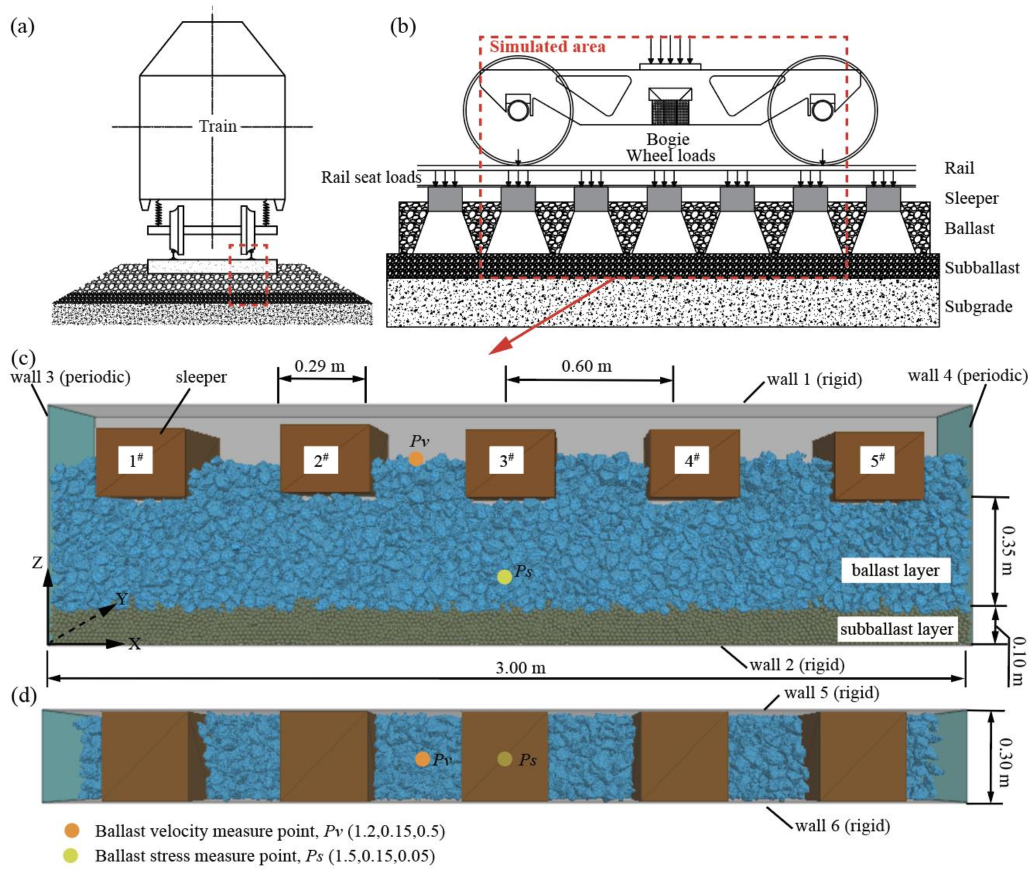

Fig. 1. Track structure: (a) transverse direction; (b) longitudinal direction; and images of the current DEM model: (c) front view; and (d) top view

The wheel load is transferred from rails to sleepers and then distributed to ballast and underlying substructure layers. Normally, one single axle load is supported by about five sleepers as reported by (Liu et al., 2017) in their field measurements. To represent the minimum representative volume element (RVE) for typical ballasted track beds, a DEM model containing five sleepers, ballast, and a sub-ballast layer is simulated in this study, as shown in Fig. 1(c) and Fig. 1(d). The model dimensions are 3.0 m in length and 0.3 m in width. It should be noted that the typical length of sleepers for a standard gauge track in Australia is about 2.4 m − 2.6 m. By exploiting double symmetry (Indraratna et al., 2011) suggested that the model transverse dimension along sleeper length is expected to be at least 0.80 m to avoid the track boundary effect. However, only 0.30 m in the transverse direction is simulated in the current DEM model considering computational efficiency. Owing to the simplification of the transverse configuration of the track bed, the influence of side slope and shoulder ballast on the dynamic response of ballasted track shown in Fig. 1(a) is not considered in this study, and the associated impacts will be discussed in later sections.Five sleepers with a cross-section of 0.29 m (wide) × 0.22 m (high) are placed at a spacing of 0.60 m and modeled by rigid wall elements in Particle Flow Code 3D (PFC3D). Underlying sleepers lie a 0.35 m-thick ballast layer and a 0.10 m-thick sub-ballast layer, which are identical to that in most ballasted tracks worldwide. To simulate the angularity and irregular morphologies of ballast aggregates, an image-aided process (Chen et al., 2019) was adopted to recreate rigid ballast clumps in the PFC3D. Fig. 2(a) and Fig. 2(b) show the polygonal meshes and the corresponding clumps of five typical ballast particles used in the current DEM analysis. The irregular shapes and angularities of ballast particles are well captured and simulated by clumps having different sizes and shapes. The particle size distribution (PSD) of ballast aggregates follows the Australian Standard AS 2758.7 (2015), as shown in Fig. 2(c). The particle size of the sub-ballast is normally in the range of 0.1 mm to 10 mm in real tracks as shown in Fig. 2(c). However, the computational resources required will be significant if there are excessively small-sized particles in the model, leading to an unacceptable simulation time. Therefore, in the current DEM analysis, the sub-ballast is scaled up and simulated by simple spheres with diameters of 10 mm. The model boundaries are simulated by rigid walls, while the two walls perpendicular to the train moving (i.e., walls 3 and 4) are periodic to represent the plane strain condition of the track.

The linear contact model is adopted for contact among particles and the required micromechanical parameters are listed in Table 1. The contact stiffnesses for particles and sleepers were determined by trial and error based on the published research (Bian et al., 2020; Indraratna et al., 2014; Li et al., 2021). For any DEM modeling, the parameter calibration of the contact model is always a complex process. When selecting the parameters for the contact model, it is necessary to balance all aspects, from macroscopic (deformation) to microscopic (stress or interparticle contact forces) responses, as well as the computational costs. Therefore, the contact model parameters were set by trial and error by referring to the study carried out on ballast at the REV level by (Chen et al., 2022). It should also be noted that wave propagation and energy accumulation are critical and inevitable problems for any FEM-based or DEM-based dynamic analysis. In the current DEM analysis, the energy dissipation is achieved by the manner of interparticle friction and global damping. The friction coefficients for ballast, subballast, and walls are 0.7, 0.5, and 0.1, respectively, and a damping coefficient with a value of 0.7 is adopted to avoid the non-physical oscillation of small-sized ballast grains and for system stability.

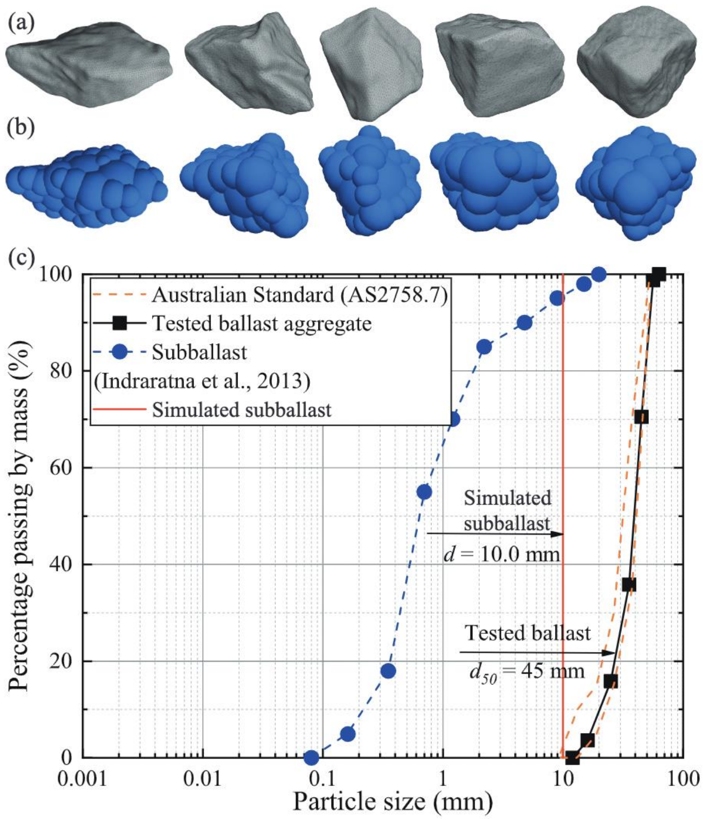

Fig. 2. Library of ballast particles: (a) polygonal meshes of ballast particles; (b) simulated rigid ballast clumps; and (c) particle size distributions in the DEM model

Table 1: Micromechanical parameters adopted for DEM simulation

Parameters	Values
Particle density (kg/m^3)	2700 (ballast/sub-ballast)
Contact stiffness for ballast, k_{nb}, k_{sb} (N/m)	1.3×10^7
Contact stiffness for sub-ballast, k_{nsb}, k_{ssb} (N/m)	5.0×10^6
Contact stiffness for walls, k_{nw}, k_{sw} (N/m)	1.7×10^7
Contact stiffness for sleepers, k_{ns}, k_{ss} (N/m)	2.1×10^7
Friction coefficient μ_b, μ_{sb} and μ_w	0.7 (ballast)/ 0.5 (sub-ballast)/ 0.1 (walls)
Local damping	0.7
Critical characteristic strength, σ_c (MPa)	10.0
Critical characteristic diameter, d_c (mm)	18.0
Pebble size scaling factor, α	0.5
Weibull modulus, m	3.4

2.2 Modeling of ballast breakage using the DEM

Upon repeated loading, it is inevitable for ballast to degrade or even split into smaller pieces, which has been investigated as primary causes of many associated problems in railways, including the differential settlement, ballast fouling, and impeded track drainage. It is reported that the predominant degradation pattern of ballast is corner breakage, although the bulk fracture of particles could be observed under high-frequency loading conditions (Sun et al., 2014). In this study, a DEM-based particle degradation subroutine developed by (Chen et al., 2022) is adopted and incorporated into the current DEM model to capture the breakage of ballast particles during train moving. Fig. 3 shows the schematic diagram of the particle degradation subroutine and algorithm that are consisted of three main modules. The degradation subroutine has been successfully implemented and validated earlier by (Chen et al., 2022; Liu et al., 2021), and the fundamental algorithm of the developed modules is briefly presented here.

- **Module 1: Potential abrasion pebble detection**

The developed particle degradation subroutine begins with detecting potential pebbles in the model that are vulnerable to abrasion and breakage during loading. All pebbles that locate on the outer contours of ballast clumps are searched and pebbles whose radii (R_p) are smaller than a radius threshold (R_c^i) are labeled as potential pebbles. The radius threshold is introduced to control the sizes of selected potential pebbles so that ballast breakage is in the pattern of corner abrasion rather than bulk fracture. It is assumed that once a particle is broken, the chance to get further breakage is significantly reduced, as the particle becomes less angular or more rounded. In this regard, the adoption of a radius threshold could prevent ballast particles from abrading limitlessly. In the current DEM study, the radius threshold (R_c^i) of a clump i is proportional to the size of the largest pebble (R_{max}^i) in the clump, as given by:

$$R_c^i = f_p \times R_{max}^i \tag{1}$$

where, f_p is the potential pebble radius threshold coefficient and is selected as 0.5.

- **Module 2: Contact force assessment**

Module 2 is developed for assessing particle breakage for which the maximum contact force failure criterion considering the Weibull strength law and particle size effect is adopted using:

$$F_c(d) = \sigma_c \left(\frac{d^{2+\alpha}}{d_c^{\alpha}}\right) \left[\ln\left(\frac{1}{P(d)}\right)\right]^{\left(\frac{1}{m}\right)} \tag{2}$$

where, $F_c(d)$ and $P(d)$ are the critical strength and the 37% survival probability for a potential pebble with a diameter of d; m is the Weibull modulus; d_c and σ_c are the characteristic diameter and the characteristic strength, which are determined via parameter calibrations. The $P(d)$ is randomly generated by 'math.random' command (written in FISH language) with the value uniformly ranging from 0 to 1. The contact forces acting on the potential pebble are captured and compared with its critical strength $F_c(d)$, and the pebble is further labeled as ready-to-break if the $F_c(d)$ is exceeded by the maximum contact forces ($F_{\max}^j$) acting on it.

- **Module 3: Pebble deletion & regeneration**

All the ready-to-break pebbles detected by **Module 2** will be automatically removed from their parent clumps to denote the corner abrasion (breakage), and newly created spheres (R_k^0) are then generated to simulate the broken fragments. To avoid applying extra forces on neighboring particles, the size of the newly created fragment sphere is scaled down by a factor of f_s with its position tangent to the parent clump as shown in Fig. 3. Subsequently, the sphere is linearly expanded by a factor of f_e to retain the mass conservation of the DEM model within a given expansion cycle (*N*). In the current DEM analysis, the value of *N* is selected as $N = 50$ to avoid the instability of the model while maintaining the mass conservation. More details on the modeling of ballast breakage using the DEM can be found by (Liu et al., 2021; Chen et al., 2022).

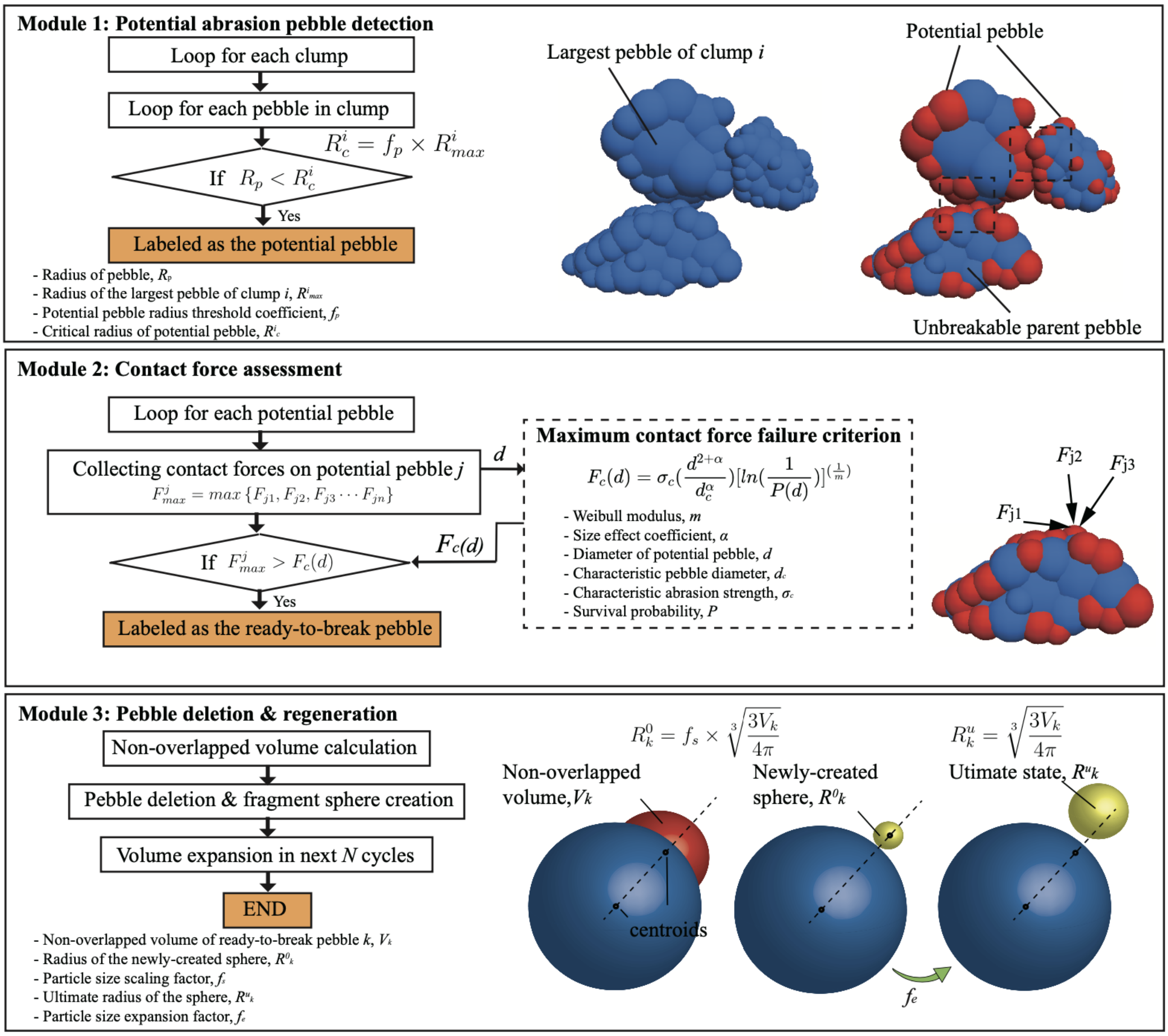

Fig. 3. Schematic diagram of ballast degradation model adopted in the DEM analysis

2.3 Modeling of moving traffic loading

To accurately capture the dynamic responses of the ballasted track under moving train loading, an 'M-shaped' stress loading pulse (Fig. 4) is simulated based on the existing vehicle-track coupled dynamic theory (Zhai, 2019). It is well known that the dynamic pressure exerted by sleepers on the underlying ballast depends on various factors, such as train speed, wheel load, wheel diameter, vehicle geometry, and overall track alignments (Esveld, 2001; Indraratna and Ngo, 2018). Nevertheless, the influence of the conditions of superstructures (i.e., wheel imperfection or rail abnormalities) and the properties of underlying ballast (i.e., the degradation of ballast) is not considered in this study, and the spectrum of the applied 'M-shaped' load for each loading scenario stayed constant during the entire simulation process. Within the scope of this DEM study, a set of properties for determining the moving train loading are selected and summarized in Table 2.

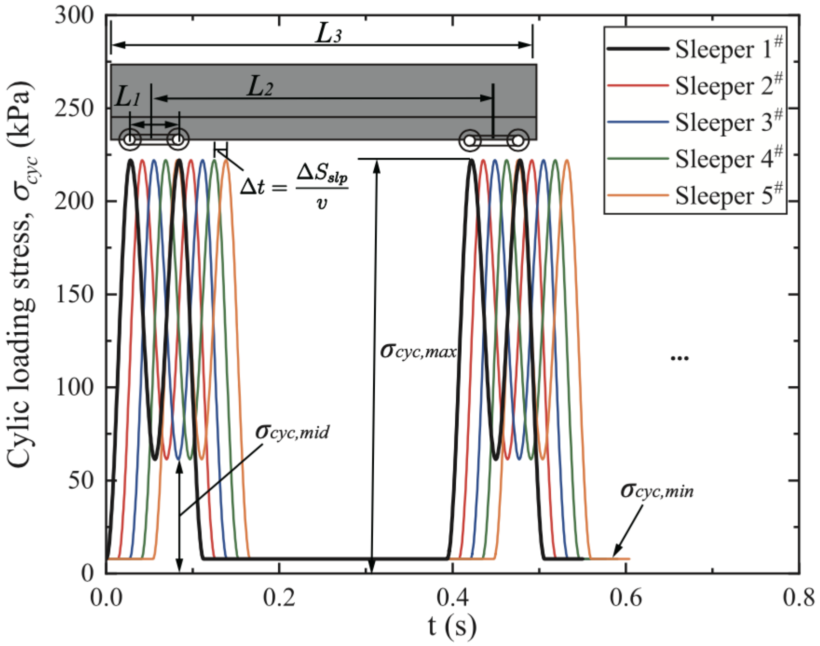

Fig. 4. Patterns of the 'M-shaped' traffic loadings applied onto different sleepers

Table 2: Properties of trains and track structures used in DEM simulation

Parameters	Values	Units
Rail mass per meter, M_R	60	kg/m
Sleeper spacing, d_s	0.6	m
Sleeper width, B_s	0.29	m
Sleeper length, L_s	2.5	m
Wheel diameter, D_w	0.97	m
Wheel distance of one bogie, L_1	2.5	m
Bogie distance of one wagon, L_2	17.5	m
Wagon length, L_3	25.5	m

Before calculating the sleeper/ballast contact pressure, the dynamic wheel load (P_d) as well the rail seat load (q_r) needs to be determined. The minimum rail seat load ($q_{r,min}$) is obtained when the track is not loaded, at which the rail seat load is mainly induced by the self-weight of fasteners and rails. Considering that the fasteners and rails on one side of the track with total masses (M_r) of 60 kg per meter are supported by concrete sleepers with base dimensions of 2.5 m (long)× 0.29 m (wide) at spacing distances (d_s) of 0.6 m, the equivalent minimum rail seat load is calculated as given by:

$$q_{r,min} = \frac{2M_r d_s g}{B_s \times L_s} \tag{3}$$

where, B_s and L_s are the width and the length of sleepers, respectively; g is the gravity unit. According to the AREA (1974), the maximum rail seat load ($q_{r,max}$) is related to the dynamic wheel load (P_d) as given by:

$$q_{r,max} = D_f \times P_d \tag{4}$$

where, D_f is the distribution factor depending on the sleeper spacings and the type of sleeper. Assuming that a wheel is acting above sleeper $3^{\#}$ (Fig. 1(c)), this wheel load will be supported by its neighboring five sleepers according to AREA (1974), distributing 10% on sleeper $1^{\#}$ and $5^{\#}$, respectively; 20% on sleeper $2^{\#}$ and $4^{\#}$, respectively; and 40% on sleeper $3^{\#}$. Therefore, the distribution factor D_f for calculating the maximum rail seat load is set to be D_f =0.4. The dynamic wheel load (P_d) is a function of the static wheel load (P_s) and the impact factor IF and it is calculated by:

$$P_d = IF \times P_s \tag{5}$$

$$IF = 1 + 5.21 \times 10^{-3} \frac{v}{D_w} \tag{6}$$

where, v is the train speed (km/h), D_w is the wheel diameter (D_w =0.97 m). By using Eq. 4~Eq. 6, the maximum rail seat load generated by wagons of different axle loads can be determined by considering the effect of train speed. Based on the field observations by (Liu et al., 2017), the rail seat load imparted on sleepers is not completely removed after the first wheel of the bogie leaves and before the second wheel approaches, and it is about 0.25 times the maximum rail seat load that the sleeper ever experiences. Therefore, the medium rail seat load ($q_{r,mid}$) when the bogie center moves above the sleeper is determined as:

$$q_{r,mid} = 0.25q_{r,max} \tag{7}$$

The rail seat load is then used to determine the contact pressure at the sleeper and ballast interface (σ_{cyc}), which is considered as the loading stresses applied onto ballast in the current DEM simulation. It is noted that the contribution of sleeper weight to contact pressure is neglected. A common approach for calculating the σ_{cyc} is to assume a uniform distribution of the q_r over an effective contact area of the sleeper, as given by:

$$\sigma_{cyc} = \left(\frac{q_r}{B_s L_e}\right) F_2 \tag{8}$$

where, L_e is the effective length of the sleeper and is assumed to be one-third of the total sleeper length by exploiting the double symmetry theory; F_2 is a safe factor depending on the sleeper type and track maintenance (Esveld, 1989; Indraratna and Ngo, 2018), and it is given as F_2 =2.0 in this study. The distances between two wheels of one bogie (L_1), the distances between centers of two bogies of one wagon (L_2), and the total length of the wagon (L_3) used in the current DEM simulation are presented in Table 2. Based on these parameters, frequencies of the applied moving train loading can be determined accordingly for various train speeds. In this study, the dynamic responses of the ballasted bed are analyzed under different magnitudes of train axle loads (i.e., 17, 20, and 25 tonnes) and train speeds (i.e., 60, 90, 120, and 150 km/h) to represent various loading conditions in real tracks. It is noted that violent vibration of superstructures (rails and sleepers) and underlying ballast can occur in actual tracks under high-speeding loading scenarios. Therefore, the train speeds in the current study are limited to low and medium levels, with the maximum speed not exceeding 150 km/h. Only five train carriages are applied in each loading scenario owing to the large computing expense.

In the existing research on the dynamic responses of ballasted tracks, there are two mainstream methods to simulate the moving wheel load generated by the passing carriages. The first one is to move an actual loading wheel back and forth directly in the test equipment, with the traveling speed of the wheel being controlled by a servo motor (Momoya et al., 2005; Ishikawa and Miura, 2015). An alternative way is to load the adjacent sleepers at a fixed phase difference via a series of hydraulic actuators attached to each sleeper (Aursudkij et al., 2009; Bian et al., 2020; Li et al., 2021). Although the former method is more direct and can consider the impact of the wheel rolling more explicitly, the speed of the loading wheel was restrained (e.g., 600 mm/min and 84 mm/min adopted by (Momoya et al., 2005, Ishikawa and Miura, 2015), respectively) owing to the limited capacity of the servo motor (or the equipment). Therefore, to simulate the fast-traveling moving loads, the time-delayed method was adopted in the current DEM analysis, at the sacrifice of ignoring the rolling-contact phenomenon as well as the caused driving torque. Ballast aggregates under two adjacent sleepers are loaded at a given time difference Δt (Fig. 4), which is equivalent to the time required for carriages with a speed of v moving from one sleeper to another one, as given by:

$$\Delta t = \frac{\Delta S_{slp}}{v} \tag{9}$$

where, ΔS_{slp} is the sleeper spacing and is 0.6 m in the current DEM model. To apply the cyclic loading, the contact forces between ballast particles and sleeper walls are measured and uniformly distributed over the entire sleeper base area. The five sleepers are forced to move upwards and downwards using a servo-controlled function to achieve the target stress levels.

2.4 Continuum stress measurement in the DEM

Due to the highly particulate nature of ballast aggregates, it is impossible to understand their responses by the commonly used continuum parameters such as stress and strain in a direct way. In this study, a subdomain method proposed by (Bagi, 1996) is adopted to interpret the particulate measurements from DEM simulations using the continuum mechanics. The local stress tensor ($\overline{\sigma_{ij}}$) of ballast aggregates is calculated by considering the contact forces acting on individual particles and the branch vectors within a group of subdomains of volume Vol_m as given by:

$$\overline{\sigma_{ij}} = \frac{1}{Vol_m}\sum_{N_c}\mathbf{F}^{(\mathbf{c})} \times \mathbf{L}^{(\mathbf{c})} \tag{10}$$

where, N_c is the number of contacts in a given subdomain; $\mathbf{F}^{(\mathbf{c})}$ is the contact force vector; $\mathbf{L}^{(\mathbf{c})}$ is the branch vector connecting the centroids of two particles in contact, as shown in Fig. 5(a). The observational process is implemented with the measuring spheres in PFC3D (Itasca, 2015).

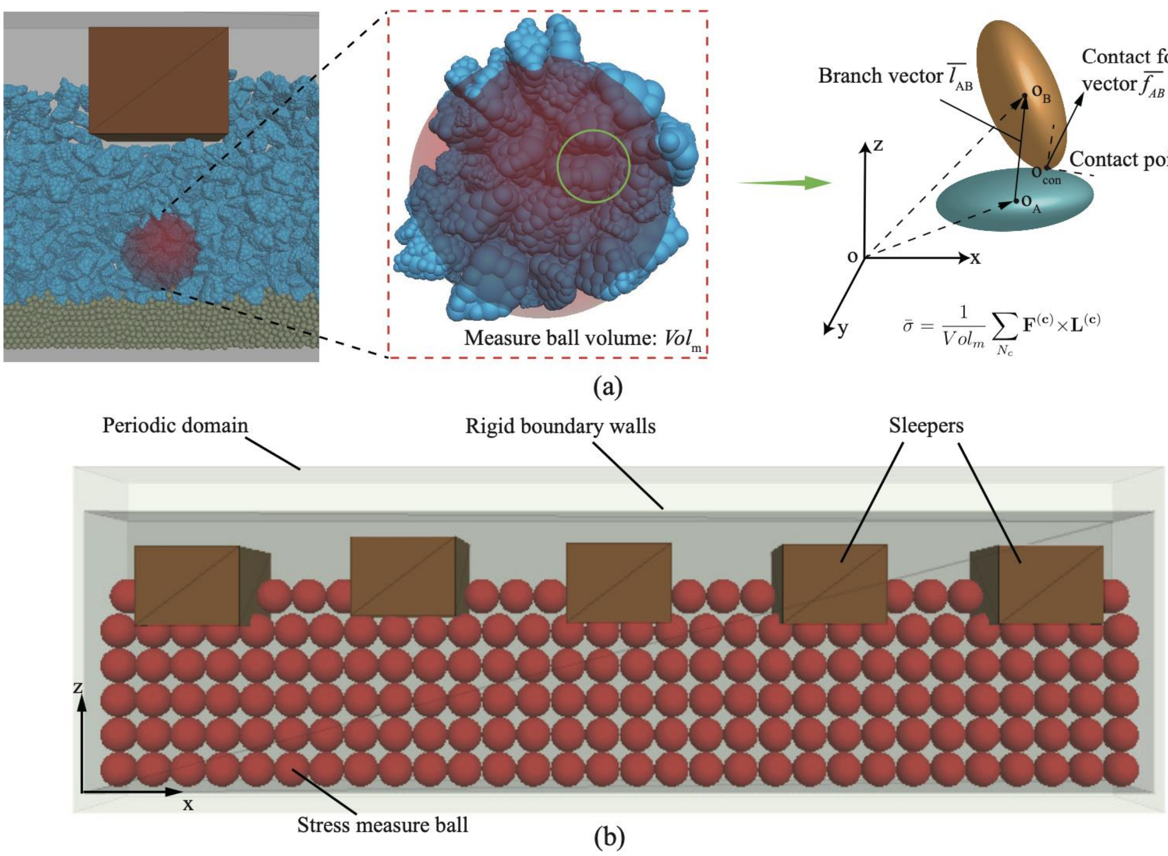

Fig. 5. (a) A typical measuring sphere and the schematic diagram of the stress tensor calculation; and (b) measuring spheres for averaged stresses in the ballast layer

To obtain the stress distributions within the ballasted bed, a cross-section parallel to the longitudinal direction of the train moving having a thickness of 0.1 m is discretized into a group of subdomains, and measuring spheres are generated to capture the averaged stresses in the ballast layer, as shown in Fig. 5(b). Then a biharmonic spline interpolation method proposed by (Sandwell, 1987) is adopted to establish the continuous stress field of the ballasted bed based on the stresses at the center of each measuring sphere.

3. Calibration of the DEM model

3.1 Verifying the stress path under moving loads with analytical solutions

Subjected to moving loading, the longitudinal and shear stresses change continuously within the ballast layer causing the principal stress axes rotation (PSR) in the plane that parallels the direction of train passage. This PSR accompanied by the continuous variation in the magnitude and orientation of the principal stress increases the complexity of stress paths in the ballast layer that has a cardioid shape in the deviatoric plane ($2\tau_{xz} \sim (\sigma_z' - \sigma_x')$), as shown in Figs. 6(a) and 6(b). To validate the developed time-delayed load moving mechanism, the stress path predicted in the current DEM simulation is firstly compared with that introduced by analytical models (Malisetty et al., 2020). It is noted that a simplified regularly shaped sinusoidal dynamic loading is adopted here instead of complex 'M-shaped' traffic loadings. Fig. 6(c) shows the variation in the deviator and shear stress measured at 0.1 m below the sleeper $3^{\#}$ during the passage of a sinusoidal loading having an amplitude of 250 kPa at a frequency of 16.6 Hz, which approximately equaled a train speed of $160\ \text{km/h}$. As the loading approached ($t < 0.05\ \text{s}$), the deviator stress ($\Delta(\sigma_z' - \sigma_x')_{cyc}$) within ballast aggregates generally increases, while the shear stress ($\tau_{xz,cyc}$) first increases to a peak value and then decreases to almost zero, at which the magnitude of $\Delta(\sigma_z' - \sigma_x')_{cyc}$ is the largest. This is expected as when the wheel reaches right above the sleeper, there would be minimum shear stress existing in ballast aggregates. During the unloading phase

($t >$ 0.05 s), the $\Delta(\sigma_z' - \sigma_x')_{cyc}$ decreases in accompany with the $\tau_{xz,cyc}$ developing in the similar trend as in the loading phase. It is also noted that the shear stress changes its sign as the loading approaches and leaves, indicating a reversed direction of $\tau_{xz,cyc}$ that in turn rotated the principal stress axes within the aggregates, as shown schematically in Fig. 6(a). The obtained stress path presented in Fig. 6(b) is basically in a cardioid shape as predicted in the analytical model (Malisetty et al., 2020). However, the stress path captured by the current DEM model is asymmetric, which could be attributed to the inhomogeneity and anisotropy of local stresses caused by the shape irregularity of ballast particles and the random packing properties of the assemblies.

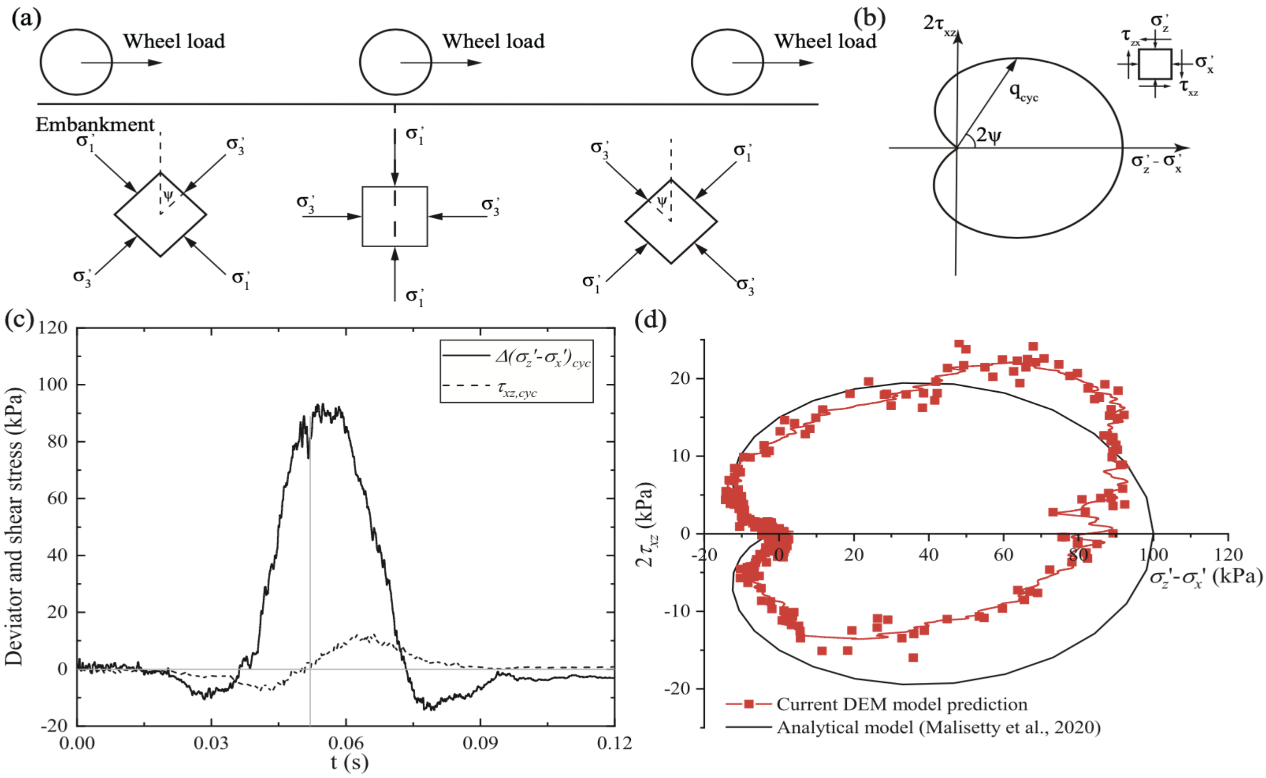

Fig. 6. (a)-(b) Analytical explanation of principal stress rotation under a moving wheel load; and (c)-(d) predicted stresses and stress path in the current DEM simulation

3.2 Comparison with field measurements

The developed ballasted track DEM model is further calibrated by comparing the dynamic stresses and vibration responses of ballast with the results measured on a full-scale track model testing facility (Bian et al., 2020). By using the ZJU-iHSRT, (Bian et al., 2020) reported the dynamic responses of a ballasted track under traffic loading conditions with an axle load of 17 tonnes and a train speed of up to 300 km/h. An ‘M-shaped’ moving train load identical to that used in the full-scale testing is applied to the current DEM model. The corresponding contact pressures between sleepers and ballast and the loading frequency are determined by Eq. 3 to 8 and then applied by a servo-control mechanism to simulate the moving loads. Two measure points, P_v and P_s (Fig. 1(c)) with their positions identical to the installed sensors in the full-scale testing are selected to monitor the velocity and the dynamic stress of ballast aggregates during simulations. Fig. 7 shows the time histories of the measured dynamic vertical stress (σ_z') and vertical vibration velocity (V_z) in the full-scale testing and the current DEM simulations. It is seen that the dynamic vertical stress σ_z' within ballast aggregates during the train passage is in an ‘M’ shape, which is in a similar pattern to the applied loading, and this behavior is well captured by the current DEM analysis. Regarding the vertical vibration velocity of ballast, obvious particle vibration is observed in both testing and DEM simulations, attributed to the effect of moving wheel loads (Zhang et al., 2017). Overall, the predicted results are in good agreement with the measured data, indicating the reliability of the developed DEM model in capturing the dynamic responses of the ballasted track under moving traffic loads.

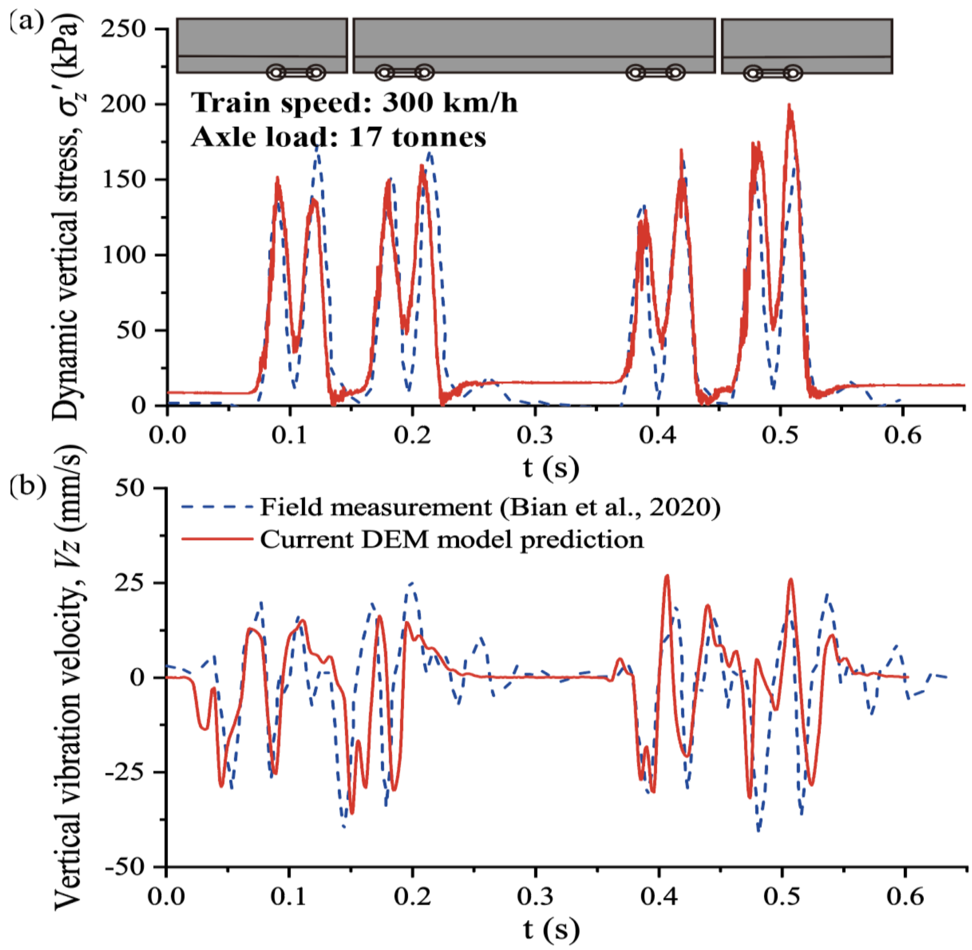

Fig. 7. Comparison between the field measurement and the current DEM model predictions in terms of: (a) the dynamic vertical stress; and (b) the vertical vibration velocity

4. Numerical results and Discussions

4.1 Dynamic responses of ballasted track

4.1.1 Settlements of sleepers

The validated ballasted track model is then subjected to a series of moving wheel loading representing different axle loads and train speeds, by which the dynamic responses of ballast under various traffic loading conditions are captured. Fig. 8(a) shows the evolution of accumulated settlements for five sleepers with the normalized moving distance (vt/L_3) during the passage of carriage groups with axle loads of 20 tonnes traveling at a speed of 120 km/h. It is seen that the variations of sleeper settlement are shaped like an ‘M’ at an evolution frequency of about 13 Hz similar to the loading frequency, indicating the one-to-one correspondence between the ballast deformation and the applied wheel loads. This observation further verified that the sampling rate adopted for measurement in the current DEM analysis is reasonable, and thereby the discussions provided in the paper based on the simulation results are reliable and convincing. The sleeper settlements (S) increase over time owing to the gradual compaction of the underlying ballast aggregates; however, this growth tends to slow down with the settlements becoming almost constant after the passing of about two carriages. In the field, thousands of train passages might be required before ballast aggregates are shaken down. The accelerated stabilization observed in the current numerical simulations is an inevitable consequence of DEM modeling because of its inherent limitations, such as limited amounts of large asperities of particle clumps and simplification in the loading patterns. In addition, owing to the fully rigid boundary conditions of the two walls parallel to the longitudinal direction of train passage and the rigid bottom boundary, the displacement of the aggregates in these directions is completely confined. In contrast, ballast aggregates in real tracks are allowed to dilate freely without fewer lateral restrictions, which results in a slower settling rate than that in DEM simulations.

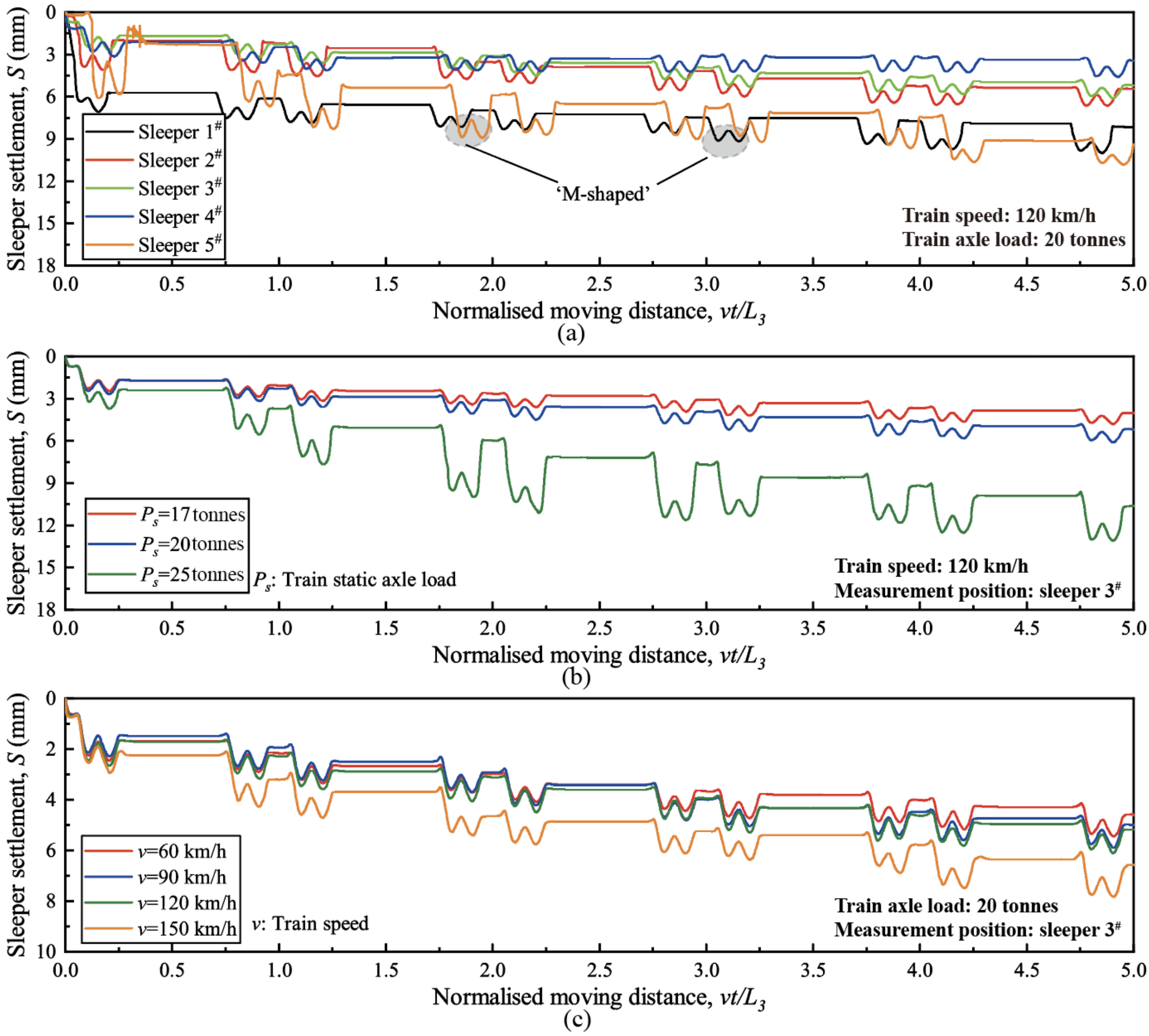

Fig. 8. Time histories of sleeper settlements predicted at various loading conditions: (a) a train with an axle load of 20 tonnes traveling at a speed of 120 km/h; (b) different axle loads; and (c) different train speeds

Considering the settlements of different sleepers, it is shown in Fig. 8(a) that the five sleepers exhibit different settling paces with distinct settlement values. This phenomenon is expected as ballast is a typical non-uniform material, the random packing and the high fabric anisotropy of the aggregates could lead to different compaction levels within the ballast layer, therefore, different settling paces are observed for the five sleepers. Moreover, it can also be found from Fig. 8(a) that sleepers close to the boundaries (i.e., sleepers $1^{\#}$ and $5^{\#}$) show greater settlements than those in the middle (i.e., sleepers $2^{\#}$, $3^{\#}$, and $4^{\#}$). As periodic conditions are applied to the boundaries close to sleepers $1^{\#}$ and $5^{\#}$, the confinement provided by ballast aggregates to the two boundary sleepers is less sufficient than that to sleepers in the model middle. Therefore, it is easier for ballast to move along the longitudinal direction of the track upon train loading, which in turn increased the settlement of sleepers $1^{\#}$ and $5^{\#}$.

To investigate the influence of axle loads and speeds on the settlement of sleepers, the time histories of the predicted settlement S for sleeper $3^{\#}$ at different loading scenarios are shown in Figs. 8(b) and 8(c). It is seen that both the axle load and the train speed affect the sleeper settlements. When subjected to higher train axle loading, the settlement of sleeper $3^{\#}$ develops in a faster trend with a greater magnitude (Fig. 8(b)), proving a more detrimental impact by heavy hauls on the settlement of ballasted tracks. As the axle load increases from 17 to 25 tonnes, the ultimate settlement of $3^{\#}$ increases from 5.31 mm to 12.58 mm after the passage of five carriages. When it comes to the train speed, it is seen from Fig. 8(c) that the sleeper settlements increase slightly at higher train speeds. The ultimate settlements merely increase from 5.45 mm to 7.83 mm when the train speeds increase from 60 km/h to 150 km/h. It should be further emphasized that the predicted settlement herein does not represent what occurred in the field case, which could be attributed to various reasons, such as the inherent imperfection of the discrete element method constitutive theory, the simplification of particle sizes and shapes, and the limitation of model boundaries. Therefore, the results are presented merely for a qualitative understanding of the dynamic responses of ballasted tracks under various moving train loading conditions.

The ultimate settlements of sleeper $3^{\#}$ (S_u) at different loading scenarios (varied axle loads and speeds) are presented in Fig. 9. Obviously, there is a high dependency between the settlement of the sleeper with the traveling speed and axle load of passing trains. However, the variations in sleeper settlements under different train speeds are less obvious compared to that under different train axle loads, implying a more profound effect of train axle load on the deformation of underlying ballast aggregates.

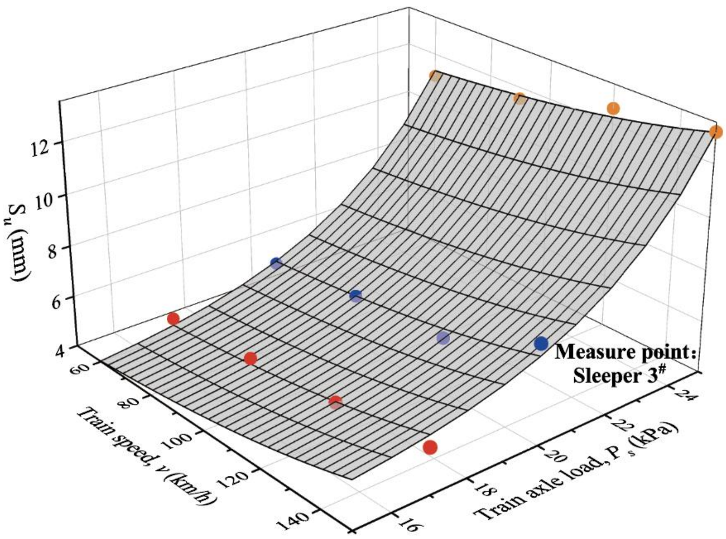

Fig. 9. Relationship between the ultimate settlement of sleeper $3^{\#}$ and the speed and the axle load of trains

4.1.2 Ballast degradation

Fig. 10(a) shows the distributions of broken ballast fragments captured from DEM simulations after the passage of five carriages with an axle load of 20 tonnes traveling at a speed of 120 km/h. As expected, the majority of fragments occur underneath sleepers because ballast in these areas directly participates in load-supporting, albeit a few broken fragments are observed in the cribs. It is found that ballast fragments are distributed within trapezoidal-shaped regions underneath sleepers. This phenomenon is supported by Ahlbeck's classic theory where rail seat loads are supposed to be transmitted within cone regions in ballast aggregates (Ahlbeck et al., 1978). The number of ballast fragments (B_f) under each sleeper is quantified and presented in Fig. 10(a). Due to the local non-uniformity and the fabric anisotropy of ballast aggregates, the number of fragments underneath different sleepers varied, indicating the non-uniform degradation levels occurred within the ballasted bed, which could be the main cause of the differential settlements that happened in rail track fields. Owing to the insufficient confinement by boundary ballast aggregates as explained earlier, the breakage of ballast particles underneath sleepers $1^{\#}$ and $5^{\#}$ is more significant than those in the middle of the model. Additionally, in areas containing a greater number of ballast fragments, a relatively larger settlement of the corresponding sleeper is observed, as shown in Fig. 8(a), which implies a direct relationship between ballast breakage and sleeper settlement. The above observation also indicates that the degradation and deformation of the ballasted bed are directly related to the lateral confinement of the aggregates. Therefore, it can be suggested methods that improve the resistance to lateral deformation for ballast, such as increasing the crib height, ought to be adopted in practical to mitigate the degradation and deformation of ballasted beds in railway tracks. It is also interesting to observe that there seem to have more ballast fragments at the two edges of sleepers than along the centrelines, for example, those underneath sleepers $1^{\#}$ and $5^{\#}$.

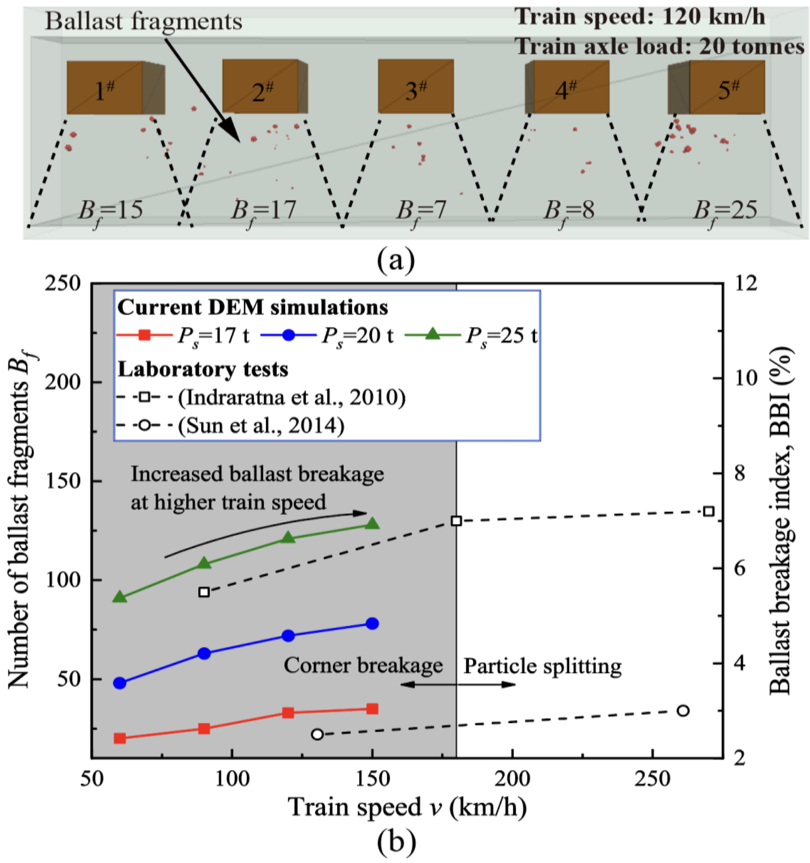

Fig. 10. (a) The distribution of ballast fragments after the passing of five carriages; and (b) evolutions of B_f and the BBI with train speeds

Figure. 10(b) shows the total number of ballast fragments that occur within the ballasted bed after the passage of five carriages with different axle loads and moving speeds. As expected, a greater value of B_f is observed for carriages with larger axle loads, indicating the more detrimental impact on ballast degradation by heavy hauls compared to the light ones. With regard to the impacts of train speed, (Sun et al., 2014) conducted a series of cyclic triaxial testing to investigate the loading frequency on the degradation of railway ballast. As a comparison, the measured ballast breakage index (BBI) from their research is also presented in Fig. 10(b). According to (Sun et al., 2014), the relationship between the loading frequency f and the train speed v can be expressed as $f = v/L$, where L is the characteristic length between axles and is given as L=2.5 m in the current DEM analysis. Therefore, the corresponding train speed value of a certain loading frequency can be obtained accordingly. It is seen from Fig. 10(b) that the predicted B_f exhibits a similar trend to the measured BBI in the laboratory testing, where an increased ballast breakage is observed at a higher train speed or loading frequency. However, the B_f shows an approximate uplift of 63% when the train speed increases from 60 km/h to 150 km/h, compared to that of about 267% when the train axle load increases from 17 to 25 tonnes, which further indicates the predominant effect of train axle load on the degradation response of ballast in railways.

By inspecting the morphologies of ballast after the cyclic loading, (Sun et al., 2014) found two main patterns for ballast breakage: (a) corner breakage, which mainly occurred at low loading frequencies ($f \leqslant 20$ Hz or $v \leqslant 180$ km/h); and (b) bulk splitting, which was observed at high loading frequencies. As the particle breakage model adopted in the current DEM simulations is developed for ballast abrasion, the bulk splitting of particles is not allowed during loading and may require further improvement of the present breakage model. Nevertheless, the predicted results obtained from the current DEM analysis are still satisfying for a given axle load and train speed.

4.1.3 Development of the dynamic stresses

The dynamic responses of the ballasted track to the train moving are further investigated in terms of the dynamic stresses develops within the ballast and sub-ballast layer. Fig. 11 presents the contour plots of the three components of dynamic stresses, the dynamic vertical stress σ'_z, the dynamic horizontal stress σ'_x, and the dynamic shear stress τ'_{xz} within the ballasted bed at three different loading stages, at which the front wheel of the first bogie with an axle load of 25 tonnes moves to sleepers $1^{\#}$, $3^{\#}$ and $5^{\#}$, respectively, at a speed of $v = 120$ km/h. It is seen that there are significant variations in the distributions of the dynamic stresses within the ballast and sub-ballast layer during train passage. As expected, an intensified σ'_z is usually observed underneath or in the vicinity of the wheels because ballast within the region support majorities of the axle loads (Figures. 11(a1)-(a3)). Owing to the train moving, ballast ahead of the carriages has been preloaded prior to the arrival of the wheels, for instance, areas underneath sleeper 2# at t = 0.038 s and sleeper 4# at t = 0.074 s. The induced stresses within ballast gradually dissipate after the wheel left; however, the axle loads by the coming rear wheels have arrived before the complete dissipation of these stresses, and the loads tend to be superposed that causing the build-up of stresses in ballast (for instance, areas underneath sleeper 2# at t = 0.110 s). Regarding the distributions of the horizontal stress (σ_x'), it varies significantly in the ballast and sub-ballast layer along the direction of the train moving similar to the development of the σ_z', and a relatively greater σ_x' is observed underneath sleepers where the train wheel moves than other areas (Figures. 11(b1)-(b3)). The largest σ_x' value emerges in ballast located at the middle part of ballast beds, as shown in Fig. 11(b2). This magnification in the σ_x' of the middle ballast layer is probably due to the elevating lateral confinement to the horizontal moving of particles within the region. Considering the distributions of the shear stress τ_{xz}' within the assemblies (Figures. 11(c1)-(c3)), it is seen that the τ_{xz}' is about symmetrically distributed with opposite signs about the centerline of each sleeper. This observation is consistent with the existing studies (Bian et al., 2020; Zhao et al., 2021).

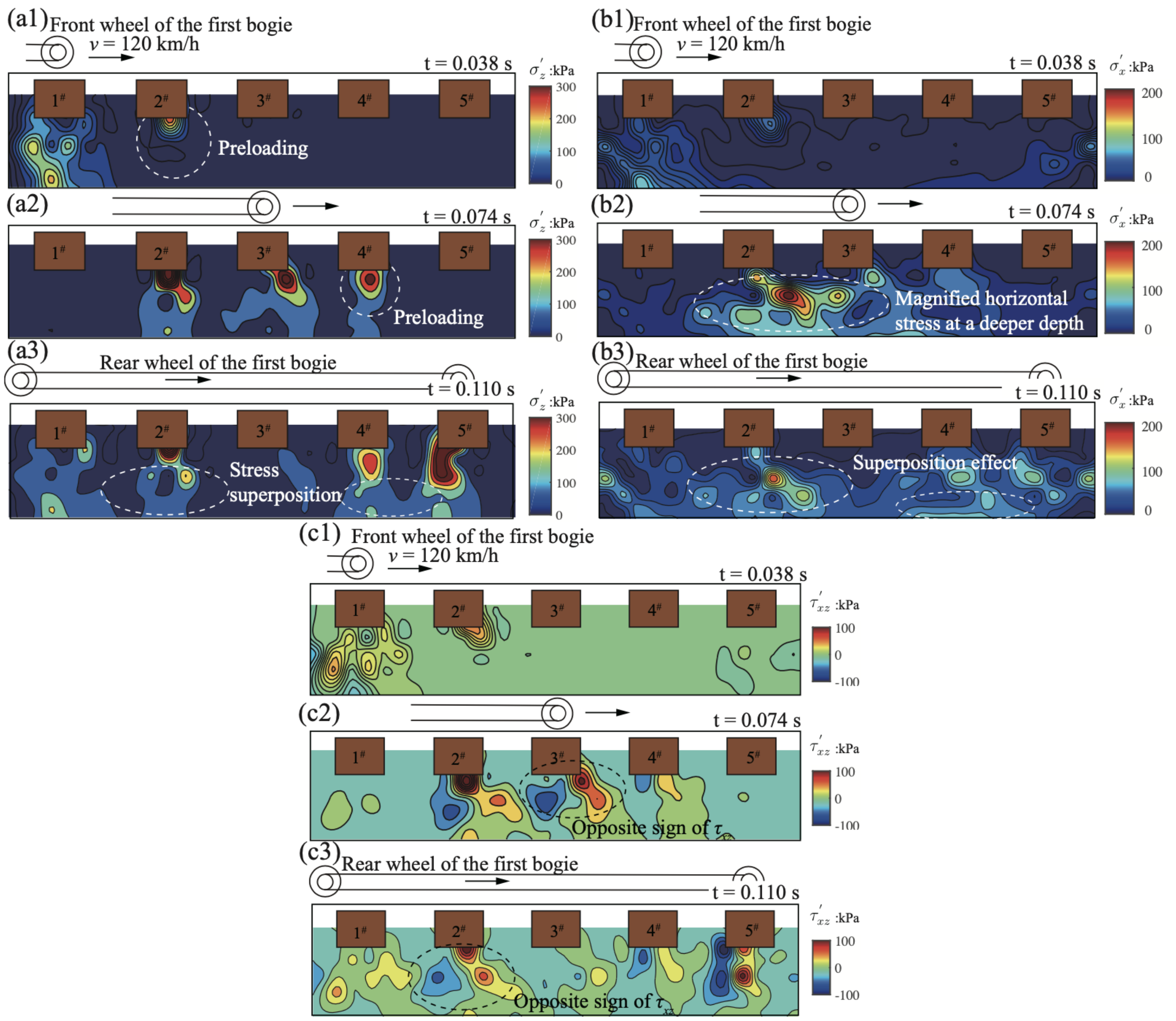

Fig. 11. Distributions of the dynamic stresses in ballast at different moving loading stages: (a1)(a2)(a3) dynamic vertical stress σ_z'; (b1)(b2)(b3) dynamic horizontal stress σ_x'; and (c1)(c2)(c3) dynamic shear stress τ_{xz}'

To further investigate the dynamic stresses developed within the ballasted bed, the evolutions of dynamic stress at different depths are monitored as the train moved. Fig. 12 shows the time histories of σ_z', σ_x', and τ_{xz}' at three different depths below the center of sleeper 3# bottom during the passage of carriage with an axle load of 25 tonnes traveling at a speed of 120 km/h. The ratio, $z/h = 0.222, 0.511, 0.778$ is for $z = 0.10, 0.23, 0.35$ m, respectively, where z is the vertical distance of the observation points to the bottom of sleeper 3#, h is the total depth of ballast and sub-ballast (h =0.45

m) in this study. The variations of the three components of dynamic stress are shaped like 'M' in response to the loading of a single bogie. This observation is consistent with the existing field measurements (Liu and Xiao, 2010), where similar trends of stress pulses within the aggregates generated by the passing trains were found. The largest values of σ_z' and τ_{xz}' are observed at the shallow ballast layer, and the σ_z' and τ_{xz}' attenuate by about 65% with the z/h increasing from 0.222 to 0.778. Considering the horizontal stress σ_x', the largest value is observed at the $z/h = 0.511$, and the σ_x' at the ballast/sub-ballast interface ($z/h = 0.778$) is significantly decreased compared to that at the z/h of 0.222.

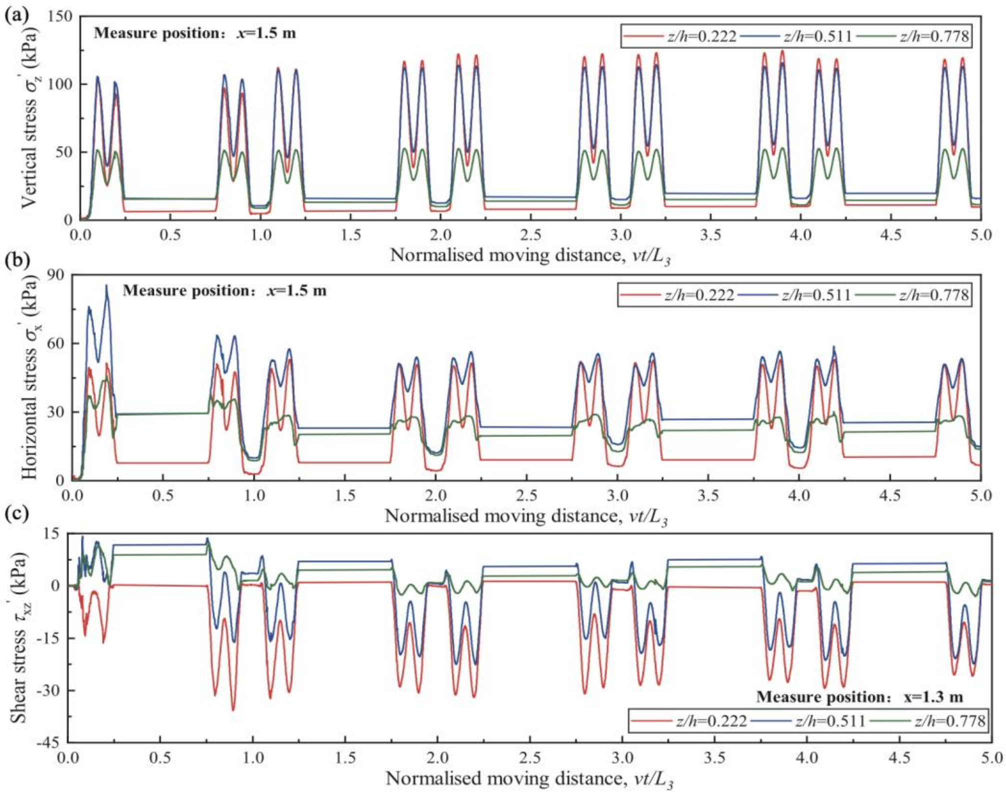

Fig. 12. Time histories of the dynamic stresses at different depths within the ballasted bed: (a) σ_z'; (b) σ_x'; and (c) τ_{xz}'

Fig. 13 presents the stress paths in the deviatoric plane that occurred in aggregates at different locations during the passage of the last bogie when a 25 tonnes-axle load carriage group travels at a speed of 120 km/h. With the approach of the front wheel, the deviatoric stress ($\sigma_z' - \sigma_x'$) in the aggregates gradually develops so as the shear stress; after the front wheel left, the $(\sigma_z' - \sigma_x')$ slightly decreases to a certain residual value and then increases with the rear wheel approaching. Moreover, similar to the induced dynamic stresses as observed in Fig. 11, the PSR in track beds is not strictly symmetrical about the centerline of each sleeper, which could be attributed to the dispersion and the local nonuniformity of ballast aggregates in DEM simulations.

To quantify the degree of principal stress rotation (PSR) that occurs in ballast, the stress axes rotation angle (ψ) which is defined as the ratio of the shear stress (τ_{xz}') in the horizontal plane to the deviatoric stress ($\sigma_z' - \sigma_x'$) by the following adopted expression (Cai et al., 2008b) is adopted:

$$\psi = \frac{1}{2}\tan^{-1}\left(\frac{2\tau_{xz}'}{\sigma_z' - \sigma_x'}\right) \tag{12}$$

From Fig. 13 it can be found that, at the three tested depths, the PSRs are insignificant along the centerline of sleeper 3# with the trajectories of the stress paths being approximately straight lines and the ψ keeping almost unchanged. By comparison, the PSRs for aggregates at sleeper edges are more obvious with the ψ continuously changing during the train passage. The simultaneous change in the magnitudes and the orientations of principal stresses and stress axes with the moving load could cause large shear deformation to the ballast. This phenomenon also explained the severer breakage of ballast particles at two edges of sleepers, as observed in Fig. 10 (a). Therefore, it can be derived from the above observation that ballast at sleeper edges would be more vulnerable to shear failure than those located underneath sleeper bottom during their service life, and the PSR occurred during train passage plays a detrimental effect on the breakage of ballast aggregates in ballasted tracks.

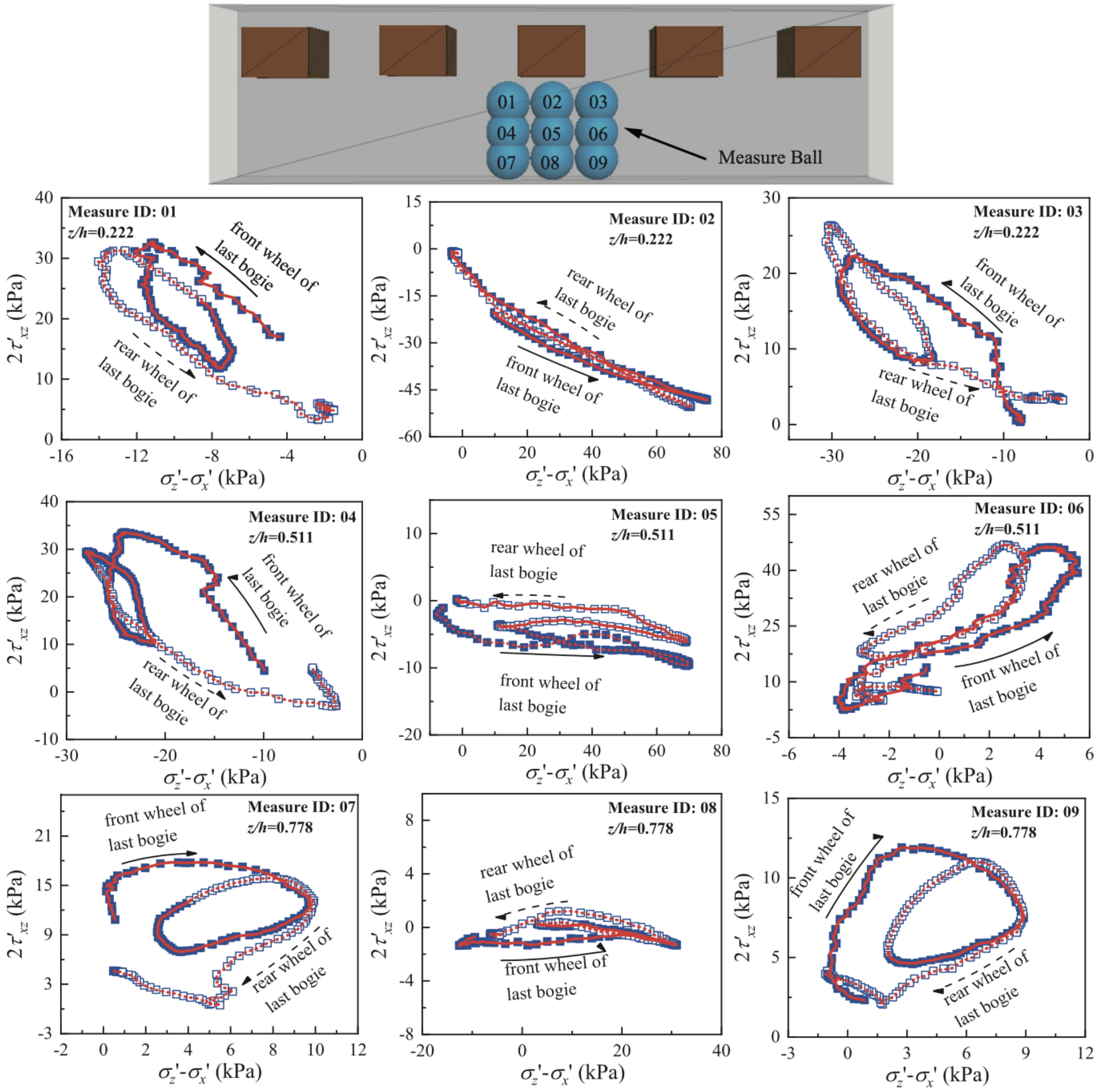

Fig. 13. The predicted stress paths in $2\tau'_{xz} \sim (\sigma'_z - \sigma'_x)$ space within the ballast and sub-ballast layer during the passage of the last bogie

4.2 Microscopic analysis of ballasted track

4.2.1 Interparticle contacts

Fig. 14 shows the development of contact chains in the ballasted bed at three typical loading phases when a train carriage group with an axle load of 25 tonnes travels at a speed of 120 km/h. During the train passage, strong contact force chains always develop underneath or in the vicinity of the wheels to directly support the imparted axle loads. The contact pressures at the sleeper/ballast interface are transmitted mainly within a trapezoidal-shaped region in the ballasted bed, which coincides with the distribution of the broken ballast fragments (Fig. 10(a)). This observation is in agreement with the classical ballast vibration model proposed by (Ahlbeck et al., 1978). The interparticle contact forces in the crib area are less intensified than those under sleepers. This is expected as the main function of crib ballast in track beds is to provide lateral resistance rather than bearing upper train loads. With train movement, the number of interparticle contacts and the averaged contact forces (f_{ave}) increase, which implies that the ballasted bed gradually become compacted under repeated train loading.

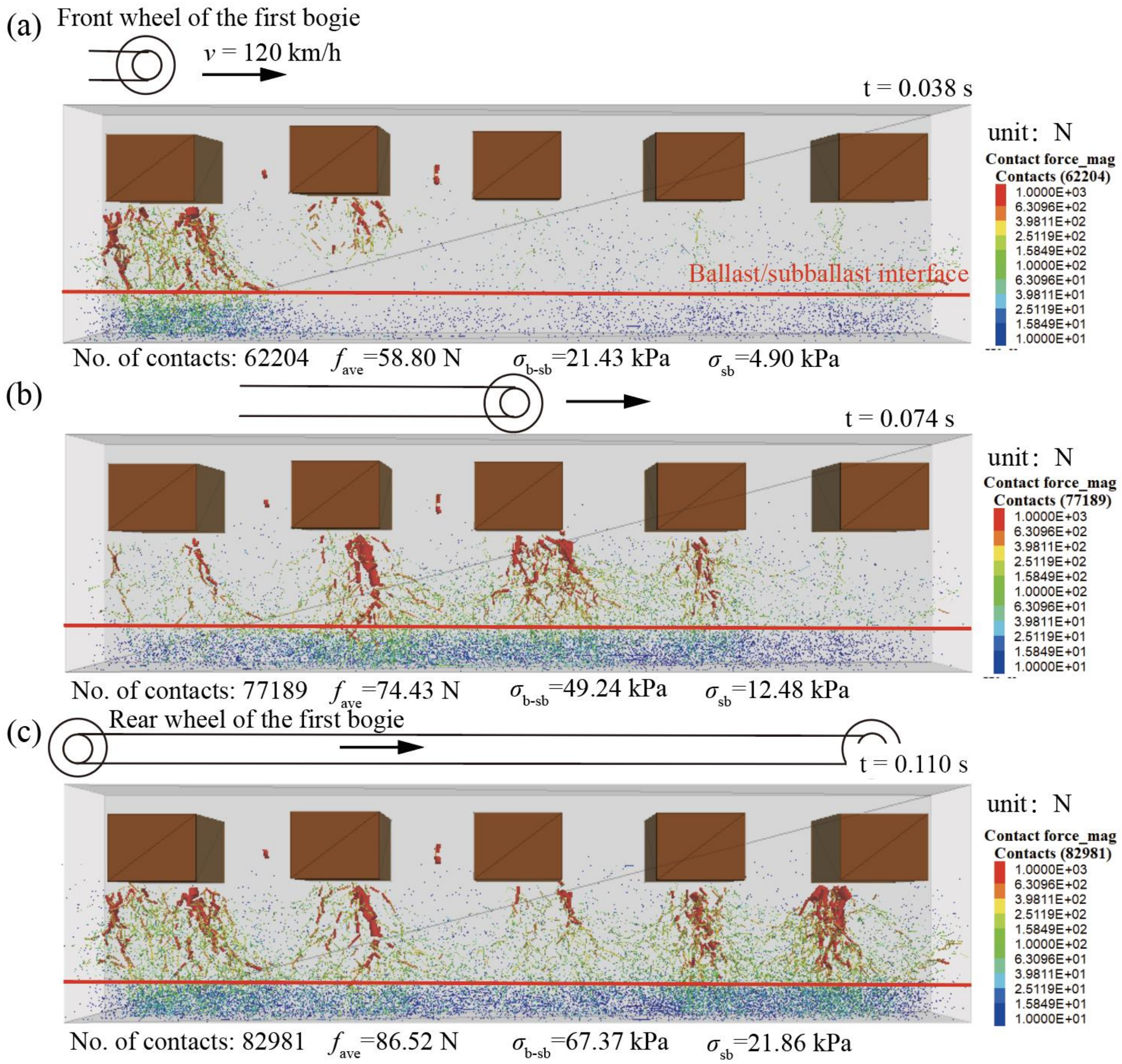

Fig. 14. Distributions of the inter-particle contact forces in the ballasted bed at different moving loading stages: (a) t=0.038 s; (b) t=0.074 s and (c) t=0.110 s

It is also seen from Fig. 14 that the interparticle contact forces attenuate along with ballast depth as the contact chains become thinner and less intensified. The nominal contact pressures at the ballast/sub-ballast interface (σ_{b-sb}) and sub-ballast bottom (σ_{sb}) are also calculated for each loading phase as presented in Fig. 14. The σ_{b-sb} and the σ_{sb} is defined as the ratio of the total contact forces at the ballast/sub-ballast interface or at the sub-ballast bottom to the area of the model base. After traveling through the 100-mm thick sub-ballast, the contact pressures decrease by approximately 68% to 77%. This observation proves that the sub-ballast decreases the traffic-induced stress transmitted to the subgrade layer in the ballasted track.

To further investigate the effect of the capping layer for ballasted tracks, the σ_{b-sb} and the σ_{sb} at $t = 0.074$ s under different loading conditions are obtained and presented in Fig. 15. Fig. 15 (a) shows the predicted values of σ_{b-sb} and the σ_{sb} under different axle loads and at the same speed ($v = 120$ km/h). As expected, the contact pressures at both the ballast/sub-ballast interface and the sub-ballast bottom increase with an increase in axle load. Nevertheless, the σ_{sb} shows merely 36.2% uplift when the train axle load increases from 17 to 25 tonnes, by contrast, a 41.6% increase is found in the σ_{b-sb}. This further indicates that the capping layer plays an important role in alleviating the disturbance by upper moving trains to the underlying subgrade. Considering the impact of train speed, it is shown in Fig. 15 (b) that the σ_{b-sb} and the σ_{sb} are the smallest at the speed of 60 km/h, and they increase significantly when the train speed is increased to 90 km/h. However, there seems to exist a critical speed after which the contact pressures at two interfaces are kept almost constant with slight variations, implying a limited effect of train speed on the induced dynamic stress within the ballasted bed.

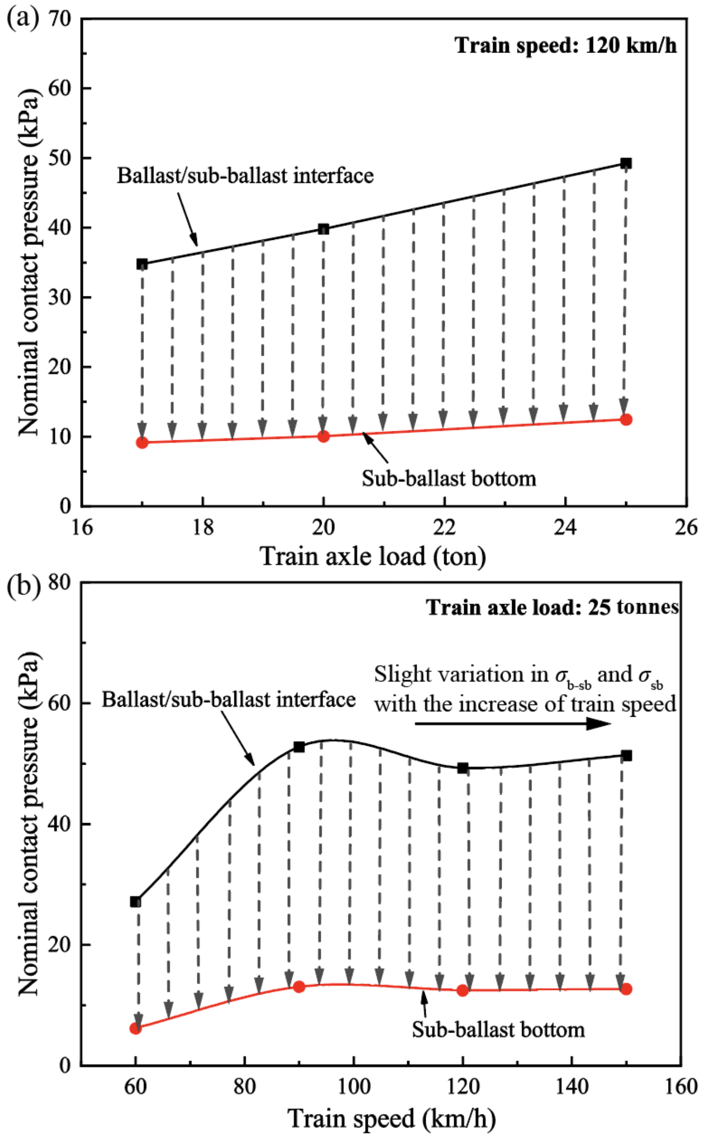

Fig. 15. The nominal contact pressure at the ballast/sub-ballast interface and the sub-ballast bottom for (a) trains of different axle loads traveling at 120 km/h; and (b) trains of an axle load of 25 tonnes traveling at different speeds

4.2.2 Predicted vibration of ballast vibration

The vibration of ballast particles during the train passage is investigated in the current study. Fig. 16(a) shows the predicted velocities of ballast and sub-ballast when carriages with axle loads of 25 tonnes travel to sleeper $3^{\#}$ at a speed of 120 km/h. Underneath the sleepers where the wheel is or is about to approach, the ballast exhibits relatively larger velocities as loaded directly by the sleepers. In addition, the crib ballast also shows considerable vibrations owing to the free surface of ballasted beds, which could cause hazardous splashes during train moving and bring serious threats to the stability of the track structure. Detailed snapshots of the vibration velocities of ballast at three different locations are shown in Fig. 16. Under train loading, the ballast underneath the wheel (Area 2) exhibits downward moving, and it pushes the ballast in front of the wheel (Area 3) to move horizontally; however, the horizontal movement of the ballast behind the wheel (Area 1) is less obvious as affected by the approaching rear wheel.

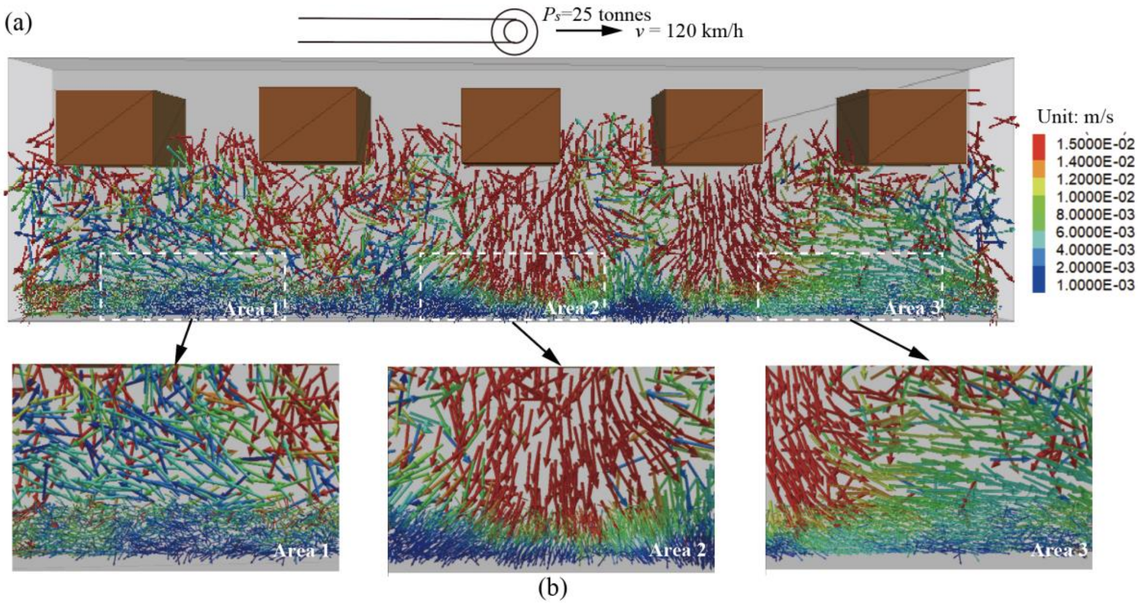

Fig. 16. Distributions of particle velocities within the ballasted bed when a train with an axle load of 25 tonnes and a speed of 120 km/h traveled to sleeper $3^{\#}$

Fig. 17(a) shows the average and the three components of ballast vibration velocity captured from DEM simulations when train carriages with different axle loads travel to sleeper $3^{\#}$ at a speed of 120 km/h. Under the three tested axle loads, the vibration velocity of ballast shows little variation, implying a minor role of train axle load in affecting ballast vibration. In contrast, the vibration of ballast is significantly affected by the train speed, with the vibration velocity of ballast being elevated from 5.01 mm/s to 10.12 mm/s when the speed of a 25-tonnes train carriage is raised from 60 km/h to 150 km/h, as shown in Fig. 17(b). Despite the limited impacts of train speed on interparticle contacts, the induced high level of ballast vibration could accelerate the compaction of ballasted beds and increase the possibility of ballast breakage. Therefore, a greater sleeper settlement and an increasing number of ballast fragments are observed at higher train speeds. Among the three components of ballast vibration velocity, the vertical velocity (vel_z) is predominant, followed by the horizontal velocity (vel_x). The lateral expansion of ballast in the direction parallel to sleeper transverse is fully restricted owing to the applied rigid boundaries, therefore, relatively small values of vel_y are observed for all the loading scenarios.

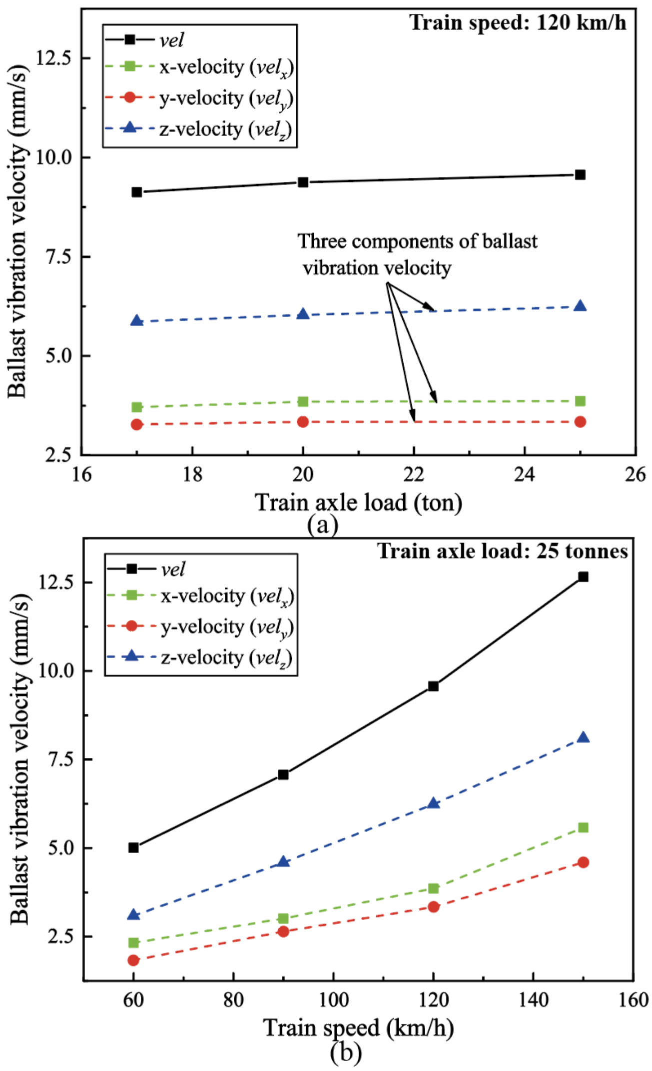

Fig. 17. Averaged velocities of ballast particles under various loading conditions

5. Limitations

The DEM modeling presented in this study simulated the dynamic responses of a ballasted track under various moving train loading. It is also noted that the current analysis still has some limitations as follows which require improvement in the future:

(1) The degradation model used in the current DEM analysis can only capture the corner abrasion of ballast particles (corner breakage). Therefore, a new DEM model simulating the bulk splitting of ballast needs to be developed in the future to serve high-frequency loading scenarios.

(2) This study aimed at low- and medium-speed trains, and the maximum train speed simulated was 150 km/h. In future research, it is suggested to develop an advanced analytical model that can consider the natural vibration of the structure to examine the dynamic responses of ballasted tracks under high-speed train loading more effectively.

(3) In the current DEM model, only a 0.30 m-wide rectangular section along the transverse direction of one rail side was simulated owing to the limited computational resources. A larger-sized model needs to be developed in future studies to consider the influence of side slopes and shoulder ballast more properly.

(4) Due to the simplification of the DEM model, the inherent imperfection of the discrete element method constitutive theory, and the dispersion of ballast aggregates, the simulation results obtained in the current DEM study may, to some extent, not be

quantitatively similar to the observation made in the field. Therefore, the results can only be understood in a qualitative way, and more advanced computational techniques need to be utilized or developed in the future to quantitatively study the dynamic responses of ballasted tracks under moving loading conditions.

6. Conclusions

This paper has discussed results obtained from a DEM modeling to study the dynamic responses of ballasted beds under moving train loading. DEM models simulating an actual ballasted track substructure were generated and calibrated by measured data from full-scale laboratory testing. A DEM-based particle breakage model was adopted and incorporated into the current DEM analysis to capture the corner abrasion and breakage of ballast. A series of moving train loading having various axle loads and speeds were simulated to investigate the load-deformation responses of ballasted tracks from both macro and microscopic perspectives. Based on the DEM results, the following conclusions could be drawn:

1. The settlement of sleepers and the breakage of ballast became exacerbated under heavier and faster train loading. However, when the train speed approached 150 km/h, the sleeper settlement and the number of ballast fragments exhibited merely a slight increase, implying that the deformation and the degradation (breakage) of ballast respond less sensitively to the variation in train speed compared to that of axle wheel load.

2. The dynamic stresses on the ballast underneath and the vicinity of the bogie wheels were

intensified during train movement, but they were gradually attenuated with depth. The magnitudes and the directions of induced dynamic stress changed continuously and cause significant principal stress rotation in the ballasted track during train movement. The ballast located at the sleeper edges showed a more profound principal stress rotation with a higher vulnerability to shear failure during service life. This further implies that due to the higher level of PSR for ballast at the sleeper edges, the particle degradation was also expected to be higher compared to the centerline of the sleeper.

3. Upon train loading, the contact pressures at the sleeper/ballast interface were transmitted within a trapezoidal region in the ballasted bed, and the intensities of interparticle contact chains became stronger when subjected to heavier trains traveling at higher speed. An attenuated interparticle contact force was observed along with ballast depth. The results proved that the capping layer could help to reduce the traffic-induced stress transmitted to the subgrade layer by approximately 68% - 77%.

4. During train passage, the crib ballast showed considerable vibrations owing to the free surface of the ballast layer, and this could cause hazardous ballast splashes on railway tracks. The axle wheel loads had minor impacts on the vibration of ballast, which was significantly affected by the speed of the train. The vibration velocity of ballast was increased from 5.01 mm/s to 10.12 mm/s when the speed of a 25-tonnes train carriage was raised from 60 km/h to 150 km/h. In reality, this implies that the increase in the magnitude of ballast vibration could accelerate the compaction of the ballast, and therefore raise the intensity of breakage of ballast aggregates.

Despite the limitations, the authors believe that the current DEM analysis provided valuable information and reference for the design optimization and the daily maintenance of ballasted tracks from both practical and theoretical perspectives.

Declarations

Data Availability

The data used to support the findings of this study are available from the corresponding author upon request.

Conflicts of Interest

The authors all declare no conflict of interest.

Acknowledgments

This work was financially supported by the Chinese Scholarship Council (No. 201906270149); and the support of the ARC Industrial Transformation Training Centre, ITTC-Rail at the University of Wollongong. The support is gratefully acknowledged.

References

Ahlbeck, D., Meacham, H., Prause, R., 1978. The development of analytical models for railroad track dynamics. In: Railroad Track Mechanics and Technology. Elsevier, 239–263. https://doi.org/10.1016/B978-0-08-021923-3.50017-6

Aursudkij, B., McDowell, G. R., Collop, A. C., 2009. Cyclic loading of railway ballast under triaxial conditions and in a railway test facility. Granular Matter 11 (6), 391–401. https://doi.org/10.1007/s10035-009-0144-4

Bagi, K., 1996. Stress and strain in granular assemblies 22 (3), 165–177. https://doi.org/10.1016/0167-6636(95)00044-5

Bian, X., Jiang, J., Jin, W., Sun, D., Li, W., Li, X., 2016. Cyclic and postcyclic triaxial testing of ballast and subballast. Journal of Materials in Civil Engineering 28 (7), 04016032. https://doi.org/10.1061/(ASCE)MT.1943-5533.0001523

Bian, X., Li, W., Qian, Y., Tutumluer, E., 2020. Analysing the effect of principal stress rotation on railway track settlement by discrete element method 70 (9), 803–821. https://doi.org/10.1680/jgeot.18.P.368

Cai, Y., Sun, H., Xu, C., 2008a. Response of railway track system on poroelastic half-space soil medium subjected to a moving train load. International Journal of Solids and Structures 45 (18-19), 5015–5034. https://doi.org/10.1016/j.ijsolstr.2008.05.002

Cai, Y., Sun, H., Xu, C., 2008b. Three-dimensional analyses of dynamic responses of track–ground system subjected to a moving train load. Computers & Structures 86 (7-8), 816–824. https://doi.org/10.1016/j.compstruc.2007.07.001

Chen, J., Gao, R., Liu, Y., 2019. Numerical study of particle morphology effect on the angle of repose for coarse assemblies using DEM. Advances in Materials Science and Engineering 2019, 1–15. https://doi.org/10.1155/2019/8095267

Chen, J., Vinod, J. S., Indraratna, B., Ngo, N. T., Gao, R., Liu, Y., 2022. A discrete element study on the deformation and degradation of coal-fouled ballast. Acta Geotechnica. https://doi.org/10.1007/s11440-022-01453-4

Cundall, P., Strack, O., aug 1979. A discrete numerical model for granular assemblies. International Journal of Rock Mechanics and Mining Sciences & Geomechanics Abstracts 16 (4), 77. https://doi.org/10.1680/geot.1979.29.1.47

Esveld, C. (1989). Modern Railway Track. MRT Productions.

Feng, B., Park, E.H., Huang, H., Li, W., Tutumluer, E., Hashash, Y.M.A., Bian, X., 2019. Discrete Element Modeling of Full-Scale Ballasted Track Dynamic Responses from an Innovative High-Speed Rail Testing Facility. Transp. Res. Rec. J. Transp. Res. Board 036119811984647. https://doi.org/10.1177/0361198119846475

Gräbe, P.J., Clayton, C.R., 2009. Effects of Principal Stress Rotation on Permanent Deformation in Rail Track Foundations. J. Geotech. Geoenvironmental Eng. 135, 555–565. https://doi.org/10.1061/(ASCE)1090-0241(2009)135:4(555)

Huang, H., Tutumluer, E., Dombrow, W., 2009. Laboratory characterization of fouled railroad ballast behavior. Transportation Research Record: Journal of the Transportation Research Board 2117 (1), 93–101.

Indraratna, B., Salim, W., Rujikiatkamjorn, C., 2011. Advanced Rail Geotechnology - Ballasted Track. Taylor & Francis Ltd.

Indraratna, B., Ngo, N. T., Rujikiatkamjorn, C., 2013. Deformation of coal fouled ballast stabilized with geogrid under cyclic load. Journal of Géotechnical and Géoenvironmental Engineering 139 (8), 1275–1289. https://doi.org/10.1061/(ASCE)GT.1943-5606.0000864

Indraratna, B., Ngo, N. T., Rujikiatkamjorn, C., Vinod, J. S., 2014. Behavior of fresh and fouled railway ballast subjected to direct shear testing: Discrete element simulation. International Journal of Geomechanics 14 (1), 34–44.

Indraratna, B., Ngo, T., 2018. Ballast Railroad Design: Smart-UOW Approach. Taylor & Francis Ltd.

Ishikawa, T., Miura, S., 2015. Influence of moving wheel loads on mechanical behavior of submerged granular roadbed. Soils Found. 55, 242–257. https://doi.org/10.1016/j.sandf.2015.02.002

Itasca, 2015. PFC3D 5.0 particle flow code in three dimensions, theory and implementation volume. Minneapolis, Minnesota.

Jing, G. Q., Ji, Y. M., Qiang, W. L., Zhang, R., 2020. Experimental and numerical study on ballast flakiness and elongation index by direct shear test. International Journal of Geomechanics 20 (10), 04020169.

Li, H., McDowell, G., de Bono, J., 2021. A new time-delayed periodic boundary condition for discrete element modelling of railway track under moving wheel loads 23 (4). https://doi.org/10.1007/s10035-021-01123-4

Liu, J., Xiao, J., 2010. Experimental study on the stability of railroad silt subgrade with increasing train speed. Journal of Géotechnical and Géoenvironmental Engineering 136 (6), 833–841. https://doi.org/10.1061/(ASCE)GT.1943-5606.0000282

Liu, Q., Lei, X., Rose, J. G., Purcell, M. L., 2017. Pressure measurements at the tie-ballast interface in railroad tracks using granular material pressure cells. American Society of Mechanical Engineers. https://doi.org/10.1115/JRC2017-2219

Liu, Y., Gao, R., Chen, J., 2019. Exploring the influence of sphericity on the mechanical behaviors of ballast particles subjected to direct shear. Granular Matter 21 (4). https://doi.org/10.1007/s10035-019-0943-1

Liu, Y., Gao, R., Chen, J., 2021. A new DEM model to simulate the abrasion behavior of irregularly-shaped coarse granular aggregates. Granular Matter 23 (3). https://doi.org/10.1007/s10035-021-01130-5

Malisetty, R. S., Indraratna, B., Vinod, J., 2020. Behaviour of ballast under principal stress rotation: Multi-laminate approach for moving loads 125, 103655. https://doi.org/10.1016/j.compgeo.2020.103655

McDowell, G. R., Lim, W. L., Collop, A. C., Armitage, R., Thom, N. H., 2005. Laboratory simulation of train loading and tamping on ballast. Proceedings of the Institution of Civil Engineers - Transport 158 (2), 89–95. https://doi.org/10.1680/tran.2005.158.2.89

McDowell, G. R., Li, H., 2016. Discrete element modelling of scaled railway ballast under triaxial conditions. Granular Matter 18 (3). https://doi.org/10.1007/s10035-016-0663-8

Momoya, Y., Sekine, E., Tatsuoka, F., 2005. Deformation characteristics of railway roadbed and subgrade under moving-wheel load. Soils and foundations 45 (4), 99–118. https://doi.org/10.3208/sandf.45.4_99

Munjiza, A.A., 2004. The combined finite-discrete element method. John Wiley & Sons.

Ngo, N. T., Indraratna, B., 2020. Analysis of deformation and degradation of fouled ballast: Experimental testing and DEM modeling. International Journal of Geomechanics 20 (9), 06020020. https://doi.org/10.1061/(ASCE)GM.1943-5622.0001783

Nishiura, D., Sakaguchi, H., Aikawa, A., 2017. Development of Viscoelastic Multi-Body Simulation and Impact Response Analysis of a Ballasted Railway Track under Cyclic Loading. Materials 10, 615. https://doi.org/10.3390/ma10060615

Nishiura, D., Sakai, H., Aikawa, A., Tsuzuki, S., Sakaguchi, H., 2018. Novel discrete element modeling coupled with finite element method for investigating ballasted railway track dynamics. Comput. Geotech. 96, 40–54. https://doi.org/10.1016/j.compgeo.2017.10.011

Punetha, P., Nimbalkar, S.S., 2022. Geotechnical rheological modeling of ballasted railway tracks considering the effect of principal stress rotation. Can. Geotech. J. https://doi.org/10.1139/cgj-2021-0562

Qian, Y., Mishra, D., Tutumluer, E., Kazmee, H. A., 2015. Characterization of geogrid reinforced ballast behavior at different levels of degradation through triaxial shear strength test and discrete element modeling. Geotextiles and Geomembranes 43 (5), 393–402. https://doi.org/10.1016/j.geotexmem.2015.04.012

Qian, J., Du, Z., Lu, X., Gu, X., Huang, M., 2019. Effects of principal stress rotation on stress–strain behaviors of saturated clay under traffic–load–induced stress path. Soils Found. 59, 41–55. https://doi.org/10.1016/j.sandf.2018.08.014

Sakaguchi, H., 2004. New computational scheme of discrete element approach for the solid earth multi-materials simulation using three-dimensional four particle interaction. Front. Res. Earth Evol. 2, 1–5.

Sandwell, D. T., 1987. Biharmonic spline interpolation of GEOS-3 and SEASAT altimeter data 14 (2), 139–142. https://doi.org/10.1029/GL014i002p00139

Sayeed, Md.A., Shahin, M.A., 2022. Dynamic Response Analysis of Ballasted Railway Track–Ground System under Train Moving Loads using 3D Finite Element Numerical Modelling. Transp. Infrastruct. Geotechnol. https://doi.org/10.1007/s40515-022-00238-2

Selig, E., Waters, J., 1995. Track Geotechnology and Substructure Management. Thomas Telford Publishing.

Sun, Q. D., Indraratna, B., Nimbalkar, S., 2014. Effect of cyclic loading frequency on the permanent deformation and degradation of railway ballast. Géotechnique 64 (9), 746–751. https://doi.org/10.1680/geot.14.T.015

Zhai, W.M., 2019. Vehicle-Track Coupled Dynamics. Springer, Singapore.

Zhang, X., Zhao, C., Zhai, W., 2017. Dynamic behavior analysis of high-speed railway ballast under moving vehicle loads using discrete element method. International Journal of Geomechanics 17 (7), 04016157. https://doi.org/10.1061/(ASCE)GM.1943-5622.0000871

Zhao, H.-Y., Indraratna, B., Ngo, T., 2021. Numerical simulation of the effect of moving loads on saturated subgrade soil. Computers and Géotechnics 131, 103930. https://doi.org/10.1016/j.compgeo.2020.103930

List of Figures and Tables

Table 1: Micromechanical parameters adopted for DEM simulation

Table 2: Properties of trains and track structures used in DEM simulation

Fig. 1. Track structure: (a) transverse direction; (b) longitudinal direction; and images of the current DEM model: (c) front view; and (d) top view

Fig. 2. Library of ballast particles: (a) polygonal meshes of ballast particles; (b) simulated rigid ballast clumps; and (c) particle size distributions in the DEM model

Fig. 3. Schematic diagram of ballast degradation model adopted in the DEM analysis

Fig. 4. Patterns of the 'M-shaped' traffic loadings applied onto different sleepers

Fig. 5. (a) A typical measuring sphere and the schematic diagram of the stress tensor calculation and; (b) measuring spheres for averaged stresses in the ballast layer

Fig. 6. (a)-(b) Analytical explanation of principal stress rotation under a moving wheel load; and (c)-(d) predicted stresses and stress path in the current DEM simulation

Fig. 7. Comparison between the field measurement and the current DEM model predictions in terms of: (a) the dynamic vertical stress; and (b) the vertical vibration velocity

Fig. 8. Time histories of sleeper settlements predicted at various loading conditions: (a) a train with an axle load of 20 tonnes traveling at a speed of 120 km/h; (b) different axle loads; and (c) different train speeds

Fig. 9. Relationship between the ultimate settlement of sleeper $3^{\#}$ and the speed and the axle load of trains

Fig. 10. (a) The distribution of ballast fragments after the passing of five carriages; and (b) evolutions of B_f and the BBI with train speeds

Fig. 11. Distributions of the dynamic stresses in ballast at different moving loading stages: (a1)(a2)(a3)

dynamic vertical stress σ_z'; (b1)(b2)(b3) dynamic horizontal stress σ_x'; and (c1)(c2)(c3) dynamic shear stress τ_{xz}'

Fig. 12. Time histories of the dynamic stresses at different depths within the ballasted bed: (a) σ_z'; (b) σ_x'; and (c) τ_{xz}'

Fig. 13. The predicted stress paths in $2\tau_{xz}' \sim (\sigma_z' - \sigma_x')$ space within the ballast and sub-ballast layer during the passage of the last bogie

Fig. 14. Distributions of the inter-particle contact forces in the ballasted bed at different moving loading stages: (a) t=0.038 s; (b) t=0.074 s; and (c) t=0.110 s

Fig. 15. The nominal contact pressure at the ballast/sub-ballast interface and the sub-ballast bottom for(a) trains of different axle loads traveling at 120 km/h; and (b) trains of an axle load of 25 tonnes traveling at different speeds

Fig. 16. Distributions of particle velocities within the ballasted bed when a train with an axle load of 25 tonnes and a speed of 120 km/h traveled to sleeper $3^{\#}$

Fig. 17. Averaged velocities of ballast particles under various loading conditions